The EUMETSAT Network of Satellite Application Facilities

ROM SAF
Radio Occultation Meteorology

ROM SAF CDOP-2

Visiting Scientist Report 29:

Retrieval of gravity waves from RO measurements: Capacities and limitations

Sergey Khaykin

Danish Meteorological Institute (DMI)
European Centre for Medium-Range Weather Forecasts (ECMWF)
Institut d'Estudis Espacials de Catalunya (IEEC)
Met Office (METO)

Ref: SAF/ROM/DMI/REP/VS/29
Version: 1.1
Date: 14 November 2016

DOCUMENT AUTHOR TABLE

	Author(s)	*Function*	*Date*	*Comment*
Prepared by:	Sergey Khaykin	ROM SAF Visiting Scientist	14/11/2016	
Reviewed by (internal):	Johannes K. Nielsen	ROM SAF Scientist	27/10/2016	
Approved by:	Kent B. Lauritsen	ROM SAF Project Manager	14/11/2016	

DOCUMENT CHANGE RECORD

Issue/Revision	*Date*	*By*	*Description*
Draft 1	07/10/2016	SK	First draft
Draft 2	27/10/2016	SK JKN	Suggestions from JKN
Draft 3	28/10/2016	SK	Updated version after review by JKN. Editorial corrections and replotting of Figure 14.
1.0	7/11/2016	SK	Final version (after minor editorial corrections)
1.1	14/11/2016	SK	Added abstract

VS Author

The VS study was carried out by Dr. Sergey Khaykin, LATMOS-CNRS/UVSQ; Email: Sergey.Khaykin@latmos.ipsl.fr

VS Duration

The VS study was performed during June - October 2016 at the home institute of the candidate with two visits each lasting two weeks to DMI.

ROM SAF

The Radio Occultation Meteorology Satellite Application Facility (ROM SAF) is a decentralised processing center under EUMETSAT which is responsible for operational processing of GRAS radio occultation (RO) data from the Metop satellites and radio occultation data from other missions. The ROM SAF delivers bending angle, refractivity, temperature, pressure, humidity, and other geophysical variables in near-real time for NWP users, as well as reprocessed data (Climate Data Records) and offline data for users requiring a higher degree of homogeneity of the RO data sets. The reprocessed and offline data are further processed into globally gridded monthly-mean data for use in climate monitoring and climate science applications.

The ROM SAF also maintains the Radio Occultation Processing Package (ROPP) which contains software modules that aids users wishing to process, quality-control and assimilate radio occultation data from any radio occultation mission into NWP and other models.

The ROM SAF Leading Entity is the Danish Meteorological Institute (DMI), with Cooperating Entities: i) European Centre for Medium-Range Weather Forecasts (ECMWF) in Reading, United Kingdom, ii) Institut D'Estudis Espacials de Catalunya (IEEC) in Barcelona, Spain, and iii) Met Office in Exeter, United Kingdom. To get access to our products or to read more about the ROM SAF please go to: http://www.romsaf.org

Intellectual Property Rights

List of Contents

Abstract

The study addresses the problematics of gravity waves (GWs) retrieval from GNSS radio occultation (RO) measurements and projects it onto the demonstration ROM SAF CDR Version 0 data set, based on CHAMP, GRACE, COSMIC and Metop-A observations altogether spanning 14 years. A review of the existing methods for retrieving GW parameters (potential energy, wavelengths and momentum flux) as well as of their capacities and limitations is provided. After a description of the analysis applied to the ROM SAF CDR V.0, we present a new 14-year global climatology of the two essential GW parameters: potential energy and dominant vertical wavelength. The potential energy was derived for two vertical wavelength spectral ranges. The obtained geographical distribution, annual cycle and temporal variability of GW activity is interpreted under consideration of the known GW sources (flow over orography, convection, jet stream instabilities, planetary wave activity) and GW propagation or filtering in the background flow. After analysis of the statistical errors associated with different data gridding options, a set of recommendations for the future ROM SAF L2 and L3 products relevant for GW analysis is provided.

Executive Summary

The VS project pursued the following objectives:

OBJ1. To demonstrate the gravity waves retrieval algorithms using RO data and to assess their performance
OBJ2. To develop a set of requirements to the end-user RO-based gravity wave product
OBJ3. To build a global climatology of gravity wave based on the RO data record

All objectives were fully and successfully accomplished. The major outcomes of the study undertaken are:

1. Overview of the gravity wave (GW) parameters retrieval methods using RO data as well as their capacities and limitations.
2. Experimental climatological data set on selected GW parameters derived from the ROM SAF Climate Data Record V.0 (ROM SAF CDR V.0) generated in a test reprocessing done in July 2016 along with its geophysical interpretation.
3. A set of recommendation for the future ROM SAF L2 data and L3 gridded GW products.

The obtained results point out high potential of RO observations for GW analysis. A guideline for RO-based GW retrieval algorithms is provided. The gridded GW product is expected to be highly demanded by the atmospheric scientists and climate modellers.

1. Introduction

1.1 Purpose of Document

This document contains the results from the ROM SAF Visiting Scientist activity on retrieving atmospheric gravity wave parameters from Radio Occultation (RO) measurements with the following objectives: i) to demonstrate the gravity waves retrieval algorithms using RO data and to assess their performance; ii) To develop a set of requirements to the end-user RO-based gravity wave product; iii) To build a global climatology of gravity wave based on the RO data record.

The document is organized as follows: Chapter 2 provides an overview of application of RO measurements for retrieval of GW parameters and describes the methods applied in the present work, Chapter 3 describes the derived climatological dataset, Chapter 4 contains recommendations for the future ROM SAF GW data products, Chapter 5 concludes the report.

1.2 Background

The importance of atmospheric gravity waves (GW) for global atmospheric circulation, variability and structure is now well recognized [e.g. Alexander et al., 2010]. Gravity waves transport momentum and energy between different regions of the atmosphere. The momentum mostly generated in the troposphere is transported to upper atmospheric levels where GWs break or dissipate thereby transferring their momentum to the background wind – a phenomenon referred to as GW drag. A prominent example of GW drag effects in the tropical stratosphere is the quasi-biennial oscillation (QBO). The periodic zonal wind reversal can only be explained by the effect of GWs in that region [Lindzen and Holton, 1968]. The stimulation effect of GWs on QBO (wave drag) can reach up to 70% [Ern and Preusse, 2009]. The wave drag acts to slow the westerly winds above the midlatitude tropospheric jet maximum and significantly affect the northern winter climate [McFarlane, 1987]. GWs contribute also to the formation of the stratospheric polar vortex [Grarcia and Boville, 1994] and play a role in driving the summer hemisphere meridional transport [Alexander and Rosenlof, 1996].

The main sources of GWs include flow over orography, convection and imbalances in jet/fronts systems [Fritts and Alexander, 2003]. Existing at a wide range of horizontal scales and intrinsic frequencies [e.g. Holton, 1992], gravity waves and their effect on the mean flow pose a major difficulty for general circulation models. Due to insufficient spatial resolution these models cannot describe the full spectrum of waves explicitly and, hence, need parameterization to represent their effects. A recent study by [Geller et al., 2013] revealed large differences between such parameterizations and observations and pointed out the need in additional observational constraints.

A variety of observation techniques has already been applied in the research of wave disturbances in the atmosphere. Those include radiosonde and rocketsonde measurements, balloon soundings, radar and lidar observations and other remote sensing measurements [Khaykin et al., 2015 and references therein]. In the past two decades, remote sensing with occultation methods has undergone remarkable development. Signals of the Global Positioning System (GPS) are exploited by radio occultation (GPS RO) and are often

utilized for studies of GWs. In the future, the potential of these sounding techniques will most likely grow due to increasing numbers of transmitters and receiver platforms [Wickert et al., 2009]. The GPS RO technique provides atmospheric state profiles with global coverage under all weather and geographical conditions together with self-calibration ability and long-term stability. That makes GPS RO an almost perfect tool for atmospheric monitoring [Foelsche et al., 2008]. With almost 15 years availability, RO observations have become an important data source for climate studies.

Research on atmospheric waves using GPS RO data has expanded since early 2000s [Tsuda et al., 2000, Steiner and Kirchengast, 2000]. According to the linear theory of GWs, a separation between a small wave-induced fluctuation and background field has to be performed if vertical profiles of any state quantity are used for the retrieval of gravity wave parameters. The approach to determination of the background state is an important issue as it significantly affects the results of GW retrieval. The choice of method for estimating the background profile depends on the measurement technique exploited, its spatial and temporal sampling as well as on the desired set of retrieved GW parameters [Sacha et al., 2015; Schmidt et al., 2016].

The work carried out within the present ROM SAF VS project aims at assessing the existing methods of GW retrieval from RO data and creating an experimental data set on essential GW parameters (potential energy and vertical wavelength) based on 14 years of newly reprocessed ROM SAF RO data from CHAMP, COSMIC, GRACE and METOP-A satellite missions.

2. Application of RO for retrieval of GW parameters

2.1 Principal GW parameters

Gravity waves are buoyancy waves occurring in the interior of a stratified fluid, with buoyancy providing the restoring force (Archimede's principle), which opposes vertical displacements of air parcels along the slanted paths. The waves are transverse with temperature and wind pertubations, δT *and* δw being the two free parameters that oscillate for a freely propagating wave. In a general case, the dispersion relation for gravity waves is

$$\hat{\omega} = \frac{N^2(k^2+l^2) + f^2(m^2 + \frac{1}{4H^2})}{k^2 + l^2 + m^2 + \frac{1}{4H^2}} \qquad (1)$$

where $\hat{\omega}$ is intrinsic frequency (i.e., the frequency that would be observed in a frame of reference moving with the background wind ($\bar{u}$, $\bar{v}$)), $N=(g\delta \ln\theta/\ \delta z)^{1/2}$ is the buoyancy (Brunt-Vaisala) frequency with g – gravitational acceleration, θ – potential temperature, z – geometrical altitude, (k, l, m) wavenumber components in three directions, $f=2\Omega\sin\varphi$ is the Coriolis parameter (where Ω is the Earth rotation rate and φ is the latitude) and H – scale height. The Coriolis parameter corresponds to an oscillation with a period T ~ 16 h at 50° N, whereas the buoyancy period is ~5 min in the lower stratosphere. The dispersion relation relates the wave frequency to the wave's spatial characteristics (wave numbers) and to the background atmosphere properties N and $(\bar{u}, \bar{v})$. The gravity wave solutions above admit waves with a broad range of properties. For vertically propagating waves, (k, l, m) are real, and the intrinsic frequency is bounded between the Coriolis parameter and buoyancy frequency: $N > \hat{\omega} > |f|$. These waves are commonly termed *internal* gravity waves (IGW). A detailed theoretical basis on the atmospheric GWs can be found in a review by Fritts and Alexander [2003].

For high-frequency waves with $\hat{\omega} >> |f|$, for which the Coriolis force can be neglected and for which $m^2 >> 1/4H^2$, the dispersion relation (1) simplifies to

$$\hat{\omega} = N^2 \cos^2\alpha, \qquad (2)$$

where α is the angle between the lines of constant phase and the vertical.
Low frequency waves with $\hat{\omega} \sim f$, or *inertia*-gravity waves, are those for which the rotation of Earth has an important effect. An approximation to the dispersion relation for low-frequency gravity waves is

$$\hat{\omega} = N^2 \frac{k_h^2}{m^2} + f^2, \qquad (3)$$

where $k_h = \sqrt{k^2 + l^2}$ is the horizontal wave number.

For medium-frequency gravity waves ($N >> \hat{\omega} >> f$) the dispersion relation can be further simplified, which lends a valuable insight into GW properties and the effects related to changes in background wind and stability:

$$\hat{\omega} = N\left|\frac{k_h}{m}\right|, \qquad (4)$$

while the vertical wave number can now be very simply related to the background wind and stability:

$$|m| = \frac{N}{|\hat{c}_h|}, \qquad (5)$$

where $\hat{c}_h = c_h - \bar{u}_h$ is intrinsic phase speed. The equations (4) and (5) demonstrate that the vertical wavelength and intrinsic frequency are both proportional to the intrinsic phase speed $\hat{c}_h$. The level where $c_h = \bar{u}_h(z)$ is a critical level for the wave where vertical wavelength shrinks to zero. This theoretical level is never achieved in the real atmosphere and the waves break or dissipate when approaching the critical level. For example, if a stationary wave generated by the flow over a mountain range with ground-based phase speed c_h = 0 will propagate vertically in a coordinate system following the background wind and will reach critical level and break/dissipate in a directional wind shear, where u_h approaches 0. For a stationary wave the dispersion relation can be further simplified, allowing to estimate the vertical wavelength λ_z from the background wind and buoyancy frequency:

$$\lambda_z = 2\pi\frac{\bar{u}_h}{N}. \qquad (6)$$

Assuming a mean N=0.02 s^{-1} in the stratosphere [Schmidt et al., 2010] and zonal wind speed of 25 m s^{-1} in the stratosphere, one can expect a vertical wavelength of 7 km.

Horizontal λ_h and vertical λ_z wavelengths can be related to the horizontal and vertical wavenumbers: $\lambda_h = 2\pi/k_h$, $\lambda_z = 2\pi/m$. Oscillation period is related to frequency $T = 2\pi/\omega$, whereas the horizontal and vertical phase velocities are proportional to the respective wavenumbers: $c_x \equiv \omega/k_h$, $c_x \equiv \omega/m$. Following Schmidt et al. [2016] the equation (4) can be rewritten as

$$\frac{T_N}{T_{GW}} = \frac{\lambda_z}{\lambda_h}, \qquad (6)$$

with $T_N = 2\pi/N$ and $T_{GW} = 2\pi/\hat{\omega}$ as the Brunt-Vaisala period and the intrinsic period of the GW, respectively. Assuming N=0.02 s^{-1} in the stratosphere and a typical vertical wavelength λ_z of 8 km [Faber et al., 2013], the GW intrinsic period for a horizontal wavelength λ_h =500 km (high latitudes) is about T_{500} = 5.4 h and for λ_h =1600 km (tropics, [Wang and Alexander, 2010)) T_{1600} = 17.4 h.

Figure 1 illustrates a propagation of an atmospheric waves with horizontal wavelength λ_h, vertical wavelength λ_z, phase speed c_h and group speed g_h. Note that the waves travel with the phase velocity, whereas the energy is transmitted with the group velocity. In reality this means that a wave carrying momentum upward in the atmosphere, would manifest itself for a stationary observer as downward propagating phases in vertically and temporally resolved temperature or wind fields.

An important parameter that serves as a proxy for GW activity in the atmosphere is wave energy $E = E_p + E_k$, where E_p is the potential energy that can be deduced from a

temperature vertical profile and E_k is the kinetic energy that can be deduced from a wind velocity profile. The temperature and wind velocities are coupled to each other via the wave polarization equations. Linear theory of GW predicts that the ratio E_k/E_p is constant and amounts to 5/3 if the wave field is saturated [e.g. Gage and Nastrom, 1985]. In that case the total energy of GW can be evaluated by studying temperature data only [Tsuda et al., 2002]. Computation of E_p is done using the following expression

$$E_p = \frac{1}{2}\left(\frac{g}{N}\right)^2\left(\frac{T'}{\overline{T}}\right)^2, \qquad (7)$$

where T' is a temperature perturbation profile and $\overline{T}$ is a so called background temperature profile representing an unperturbed state of the atmosphere. The methods for determination of the latter are discussed in Section 2.3.

Another parameter reflecting the effects of GW on the background winds and atmospheric circulation is the vertical flux of horizontal momentum or GW momentum flux (MF), which can be computed as

$$MF = \rho \cdot \frac{\lambda_z}{\lambda_h} \cdot E_p, \qquad (8)$$

where ρ is the background density. Note that for estimation of the momentum flux one has to determine the horizontal wavelength first, which can not be obtained from a single profile and requires a minimum of two vertical profiles obtained close in time and space.

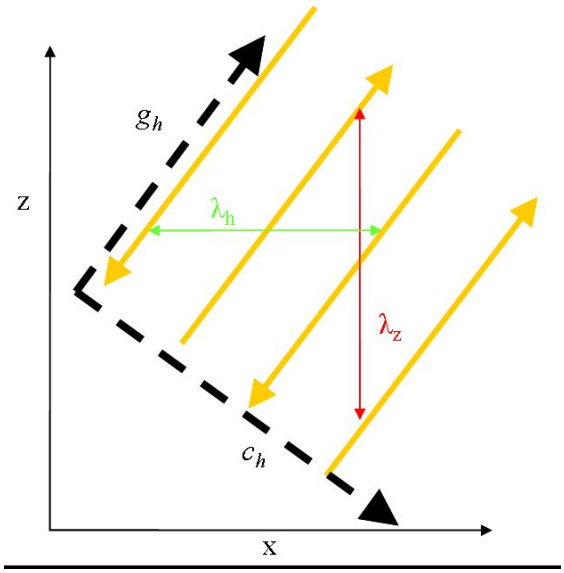

Figure 1. Schematic illustration of a propagating atmospheric wave.

2.2 Capacities and limitations of the RO-based GW retrieval

Radio occultation technique allowing for global-coverage observations of atmospheric temperature and pressure with high vertical resolution, sub-Kelvin accuracy, full diurnal coverage and all-weather capacity offers numerous advantages for studying the

atmospheric dynamics and, in particular, gravity wave activity and wave parameters. The vertical resolution of RO ranges from ~100m in the lower troposphere to 1.4 km in the upper stratosphere [Anthes et al., 2008]. The horizontal resolution is about 300 km [Kursinski et al., 1997].

As shown by Marquardt and Healy [2005], small-scale fluctuation of dry temperature RO profiles can be interpreted with certainty as gravity waves, when the vertical wavelength is equal or greater than 2 km. When the wavelengths are lower, the fluctuation may be related to noise. Alexander et al. [2008] argued that in order to keep the signal-to-noise ratio for the temperature fluctuation above the detection threshold, the analysis should be applied to the altitude range below 30 km. Nevertheless, several studies cited hereinafter use data above 30 km for retrieving GW parameters.

Generally there is no upper limit for a vertical wavelength that GW can attain through Doppler shifting in non-zero background wind. Due to the limited useful height range of RO temperature measurements (from the tropopause to 30-35 km), it is not possible to resolve waves with vertical wavelengths larger than 12-13 km. The lower limit of vertical wavelength that can be detected using RO is 2 km [Marquardt and Healy, 2005], which is determined by the Nyquist wavelength ($2\Delta x$) for the RO technique vertical resolution (i.e., sampling interval, Δx).

Based on the sensitivity studies Lange and Jacobi [2003] showed that horizontal wavelengths larger than about 100 km can in principle be detected by the RO technique. Wu et al. [2006] generalized that RO technique, as a limb sounding method, is sensitive to GWs with small ratios of vertical to horizontal wavelength. Due to the relatively low horizontal resolution and the assumption on spherical symmetry in the RO retrieval for deriving atmospheric temperature profiles, a weakening of the amplitudes and a vertical phase shift in the temperature profiles occur, whereas the strength of the effect depends on the vertical and horizontal wavelengths and the observation geometry relative to the GW field [Lange and Jacobi, 2003].

Alexander et al., [2008] concluded that wave amplitudes can be better resolved when the wave fronts are nearly horizontal or when the angle between the occultation line of sight and the horizontal component of the wave vector approaches $\pi/2$. Short horizontal scale waves have a high probability of becoming attenuated or not being detected at all. More specifically, for a uniform distribution of a wave spectrum in the range 2 km $\leq \lambda_z \leq$ 10 km and 25 km $\leq \lambda_h \leq$ 1000 km, 77% of the retrieved wave amplitudes are above 0.9 times the original ones. Another result of their study was that the detected vertical wavelengths will always differ from the original ones and only the presence of GW with nearly horizontal constant phase surfaces will result in small discrepancies.

Most of the parameters characterizing GW activity can be derived from single RO temperature profiles: temperature fluctuations T' or variances T'^2, temperature amplitude $\hat{T}$, vertical wave number m or wavelength λ_z, and potential energy E_p. Estimation of momentum flux requires the knowledge of the horizontal wave number k or wavelength λ_h, which cannot be deduced from a single temperature profile alone. For deducing the horizontal structure of GWs, it is necessary to analyze clusters of 3 or more profiles adjacent in space and time [Faber et al., 2013; Schmidt et al., 2016].

The most common GW parameter, representing a convenient proxy for estimating the wave activity is potential energy E_p, which was a focus of numerous studies cited below. It has to be kept in mind that estimation of GW potential energy is affected by the limitations of RO technique with regard to GW detection, particularly the fact that only a part of GW

spectrum can be resolved by RO. Nevertheless, comparison of GW energy estimates versus higher resolution measurements (such as radar, lidar and radiosoundings) showed reasonable agreement [Tsuda et al., 2000; Ratnam et al. 2004; Khaykin et al. 2015].

First application of radio occultation measurements for studying GW activity date back to early 2000s. Tsuda et al. [2000] used the data of GPS/MET RO mission operational 1995-1997 to infer global morphology of GWs. The next RO mission - CHAMP, operational 2001-2008, has lent its data for further studies on global GW activity [Tsuda et al., 2004; de la Torre et al., 2006; Hei et al. 2008; Schmidt et al., 2008].

Since 2006 the number of RO measurements increases dramatically after the launch of COSMIC, SACC, GRACE, TerraSat-X and METOP missions. The largest amount of data is provided by the COSMIC mission, which is based on a constellation of six Low Earth Orbiting (LEO) satellites providing up to 2000 occultations per day, which translates into one to two profiles per day in a 5° × 5° grid cell located at midlatitudes, which is where the sampling density is maximum.

A number of publications have used RO data to retrieve and analyze GW parameters. Most of them are based on COSMIC data set. S.P. Alexander [2008a] used northern hemisphere winter COSMIC data to compute GW potential energy (E_p) and pointed out generation of waves by subtropical jet stream and orography. S.P. Alexander [2008b] found on the base of COSMIC observations in the tropics an evidence of convectively generated GWs and larger scale waves interacting with the background mean flow. McDonald et al. [2010] studied geographical variation of root mean square temperature difference between pairs of COSMIC profiles and found enhancements in the regions that have been previously identified as the regions of strong GW activity associated with convection.

Wang and Alexander [2010] presented global maps of seasonal mean GW amplitude, potential energy, vertical and horizontal wavelengths and momentum flux on the base of 2006-2007 COSMIC data. Faber et al. [2013] used triplets of COSMIC temperature profiles to calculate GW momentum flux, potential energy and horizontal/vertical wavelengths. Sacha et al. [2015] studied GW activity from COSMIC density profiles and found a hotspot of wave activity above the Eastern Asia. Schmidt et al. [2016] used short-range triplets of COSMIC and CHAMP temperature profiles in 2006 to derive GW momentum flux and other wave characteristics.

In several studies RO observations were combined with other limb-viewing satellite missions or with ground based instruments. Wang and Alexander [2009] analyzed GW activity during stratospheric sudden warming events in the northern hemisphere winter using CHAMP and COSMIC data supplemented by the temperature measurements using EOS/HIRDLS and TIMED/SABER limb-viewing space-borne sounders and found consistent results on GW properties from different data sets. Wright et al (2011) compared GW analyses from HIRDLS, COSMIC and SABER and showed that, taking into account different vertical resolutions of these sounders, all of them reproduce each other's results for magnitude and vertical scales of waves in ~50 % of the cases, with COSMIC having a slightly positive frequency and temperature variance bias, presumably due to higher (than estimated) vertical resolution. Khaykin et al. [2015] combined 7 years of COSMIC RO data with OHP lidar temperature observations for analysis of GW activity distribution in the mid-latitude stratosphere at a broad altitude range and identification of GW excitation sources.

Remarkably, all aforementioned RO-based studies addressing GW climatology were either limited to a certain latitude band or covered a limited (1-2 years) time period. At present, the GPS RO data set has a time span of more than 14 years, however a complete climatology of GW parameters based on these data has not been reported in the literature yet.

3. ROM SAF experimental GW product

3.1 ROM SAF data characteristics

The GW analysis provided here is based on the ROM SAF CDR V.0 which includes reprocessed GPS RO data from the CHAMP, COSMIC, GRACE and METOP-A missions. While ROM SAF data set includes different type of files, we used the "dis" type of files (dissemination), which contains all parameters required for GW analysis: temperature, refractivity, coordinates of occultation tangent point and geometrical altitude. The data are provided on a non-regular vertical grid with a step of about 200 m (which is an oversampling for stratospheric measurements) for the vertical range between the surface and ~ 100 km. The data are archived in NetCDF format with each file containing the data from a single RO event. Among numerous parameters, the files contain the Product Confidence Data (PCD) flag, which is set for the non-nominal profiles that failed the quality check. These profiles constitute about 28% of the entire data set and are ignored in our analysis. Additionally, 0.28% of the quality-checked profiles, containing more than 3 missing values within 10-35 km range, were rejected. The total number of occultations analyzed amounts to roughly six millions.

3.1.1 Sampling frequency

Figure 2 displays the data availability expressed in total number of occultations per day as a function of time. Before the start of COSMIC mission, the RO data were provided by CHAMP only, yielding 200-300 occultations per day. In 2006, after the launch of COSMIC mission the sampling frequency increases rapidly and in 2007 it reaches 2500 occultations per day. The sampling further increases to 3000 occultations per day in 2008 with the start of METOP-A. In late 2010 the sampling frequency of COSMIC mission decreases to 1000-1500 occultations per day due to technical issues with one of the COSMIC LEO satellites and the cumulative number of occultations from all missions included in ROM SAF reprocessing varies between 1500 and 2000. At the moment of writing, COSMIC data was not yet entirely reprocessed and the year 2015 is covered by GRACE and METOP-A missions only.

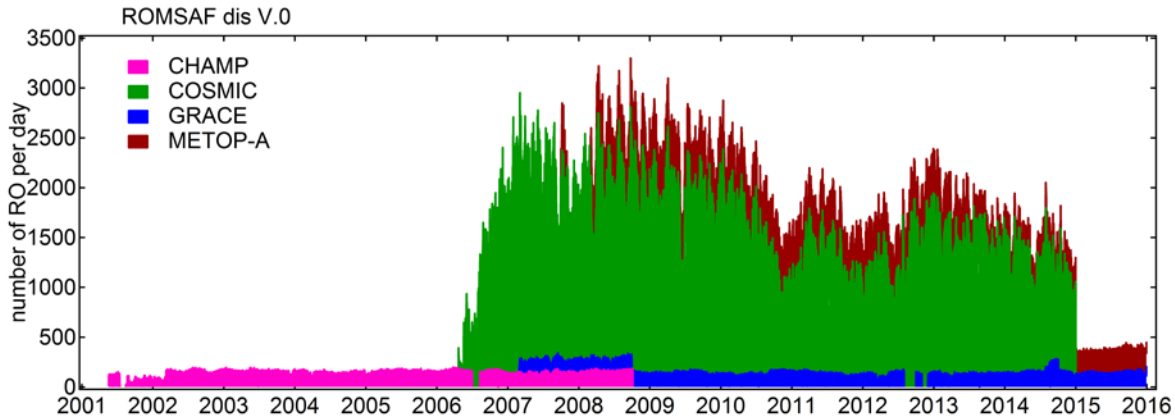

Figure 2. Cumulative number of radio occultations per day as a function of time for the ROM SAF L2 reprocessing.

Figure 3 shows geographical distribution of radio occultations performed by the four mission on a day, when the cumulative sampling was maximum (3300). The RO events are randomly distributed in space with uniform longitudinal and non-uniform latitudinal distributions. The latter is demonstrated in Fig. 4, providing the average number of occultations per year as a function of latitude for different RO missions. As can be inferred from the figure, all RO missions display similar latitudinal dependence of the sampling frequency, characterized by the primary peaks at 50°, secondary peaks at 20° and a broad minimum in the tropics. The sampling frequency decreases rapidly from mid-latitudes to the poles. It should be kept in mind though, that the sampling frequency as a function of latitude may be somewhat misleading with regard to the polar regions, which cover smaller areas of the globe.

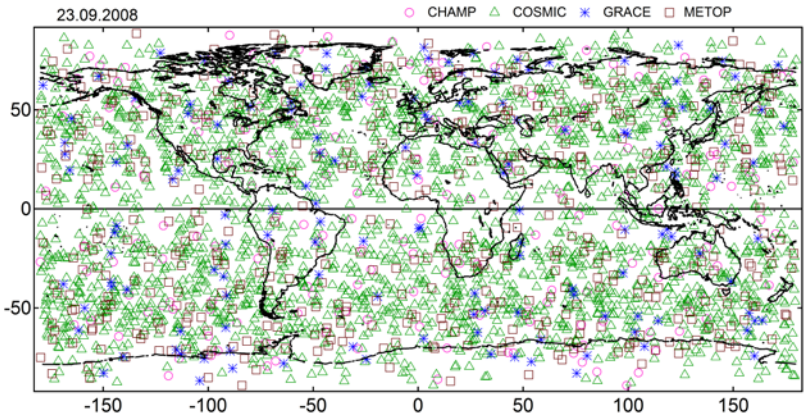

Figure 3. Geographical distribution of occultation events from different RO missions as of 23.09.2008.

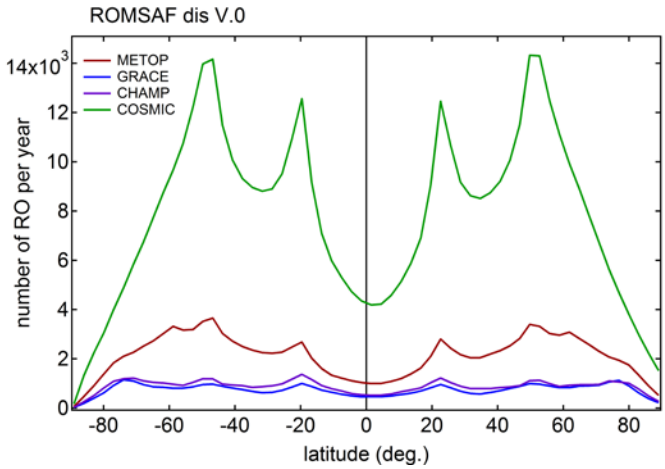

Figure 4. Latitudinal distribution of average number of occultation events per year from different RO missions.

3.1.2 Dry and wet data

The profiles of refractivity are used to generate the so-called dry and wet retrieval products. For dry air, the density profiles are first calculated using the relationship between density and refractivity. The dry temperature profiles are then derived from the density profiles based on the hydrostatic equation and the ideal gas law under the assumption that water vapor partial pressure is zero. This limits the useful range of dry profiles to stratosphere, where water concentration is low. The wet retrieval algorithm estimates both temperature and water vapor profiles using a 1D-Var algorithm with an input from model reanalysis data set.

The dissemination files, labelled "dis" include both "dry" and "wet" temperatures, wet pressure and refractivity. The dry pressure, P_{dry} can be calculated from refractivity N using the following relation [Danzer et al., 2014]

$$T_{dry} = 77.6 \cdot \frac{P_{dry}}{N} \tag{9}$$

The dry temperature, being less dependent on the model is more suitable and is commonly used for analysis of stratospheric GWs. However, we find it expedient to briefly compare the wet and dry temperature and pressure along with buoyancy frequency N^2 and GW potential energy E_p derived from the input data. For performing the comparison we analyzed COSMIC data spanning 40 days in November – early December 2008, which amounts to a total number of ~78000 occultations. Figure 5 shows vertical profiles of absolute difference between wet and dry temperature and pressure as well as the standard deviation of the differences. Comparison of temperatures reveals good agreement (<0.1 K) in the altitude range between about 15 km. Above and below those levels, the wet temperature is higher compared to the dry temperature. The standard deviation is at minimum at 13 km and gradually increases with altitude. Comparison of pressure profiles displays very low discrepancies and low variance above 23 km, whereas below that level the wet pressure becomes high-biased with respect to the dry pressure with the difference reaching 0.27 mBar at 17 km.

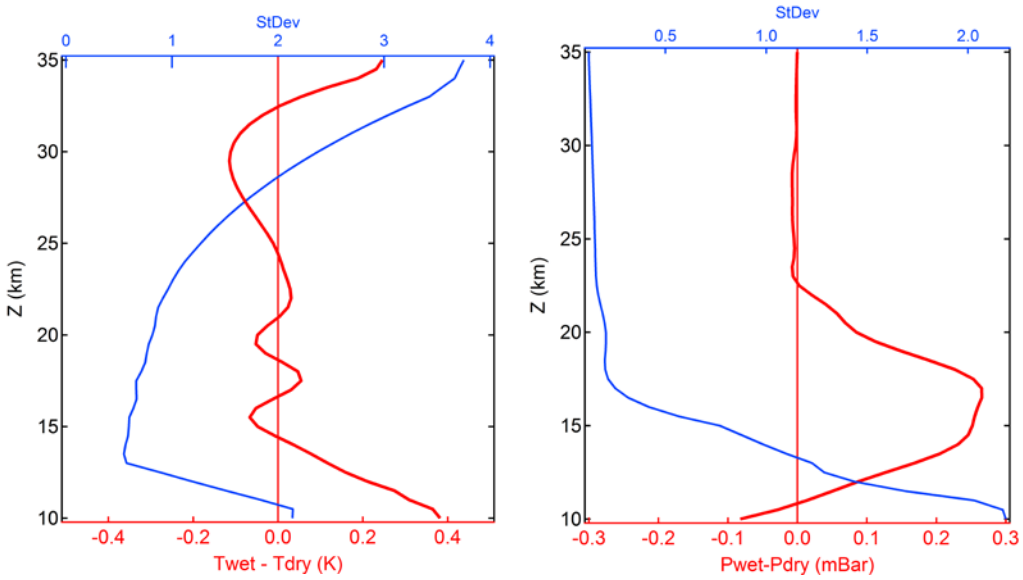

Figure 5. Comparison of dry and wet temperature (left) and pressure (right) profiles: absolute difference (red, bottom axis) and its standard deviation (blue, top axis).

An additional information on the differences between dry and wet temperatures is provided in Fig. 6, showing the latitude-altitude distribution of the differences. As can be seen, the differences show latitude dependence and asymmetric interhemispheric pattern. The largest differences are observed close to the poles, whereas the largest variation of difference with altitude is observed in the tropical lower stratosphere. Note that this pattern is based on a limited time period and may thus be different for another season.

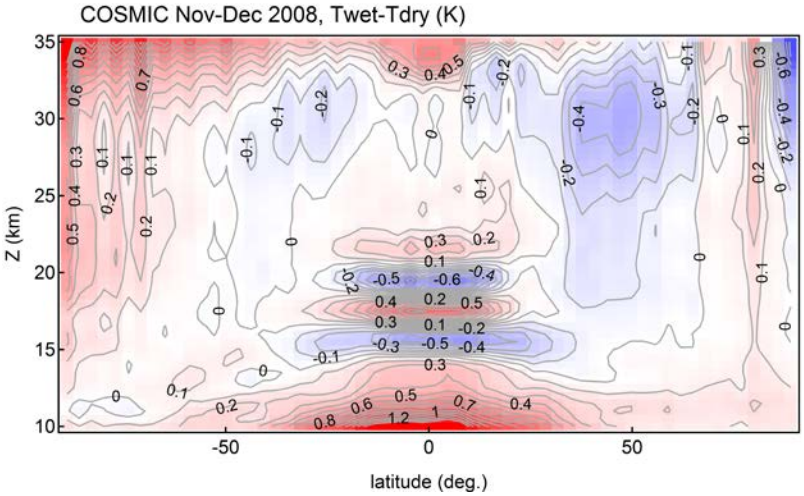

Figure 6. Latitude-altitude dependence of the zonal-mean absolute difference between wet and dry temperatures.

Figure 7 displays the comparison between dry and wet temperature and pressure for two derived parameters, E_p and N^2. The difference between dry and wet N^2 is very small and remains quasi-constant with altitude. The difference in E_p, calculated using two different methods (E_p computation methods are described in Sect. 3.2) are larger and reach 80% at 17.5 km with the dry E_p showing large values between 14 and 22 km altitude.

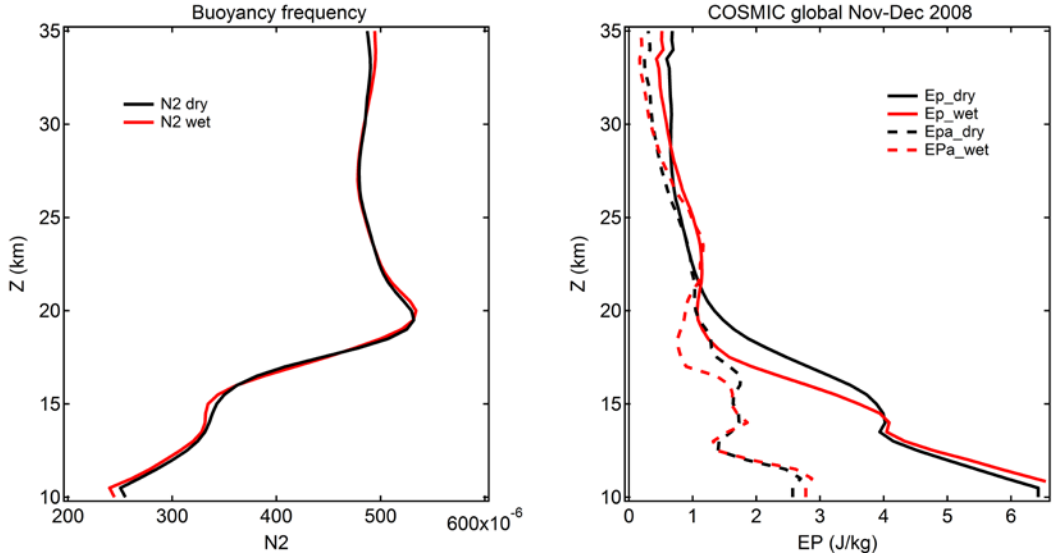

Figure 7. Comparison of buoyancy frequency (left) and GW potential energy E_p (right) derived from dry and wet temperature and pressure. E_p is calculated using horizontal (Epa) and vertical (Ep) detrending methods.

Figure 8 shows latitude-altitude section of the zonal-mean relative difference between wet and dry E_p computed using vertical detrending method. The differences exhibit an interesting pattern, characterized by three distinct altitude bands of positive and negative difference between wet and dry E_p. Since E_p is calculated using temperature perturbations, it provides a measure of fluctuations in the temperature profiles. The maximum negative difference between $E_p wet$ *and* $E_p dry$ is observed around the tropical tropopause (17-18 km), which suggests that wet temperature profiles contain less fluctuation compared to the dry profiles. The opposite is true for the red band in the middle layers of the stratosphere, which is surmounted by the second blue-coloured layer. While the interpretation of this pattern is beyond the scope of the present work, the conclusion taken out of this comparison is that dry and wet temperatures are not only different in absolute values but also in the amount of fluctuations and their amplitude in the vertical profiles of state parameters.

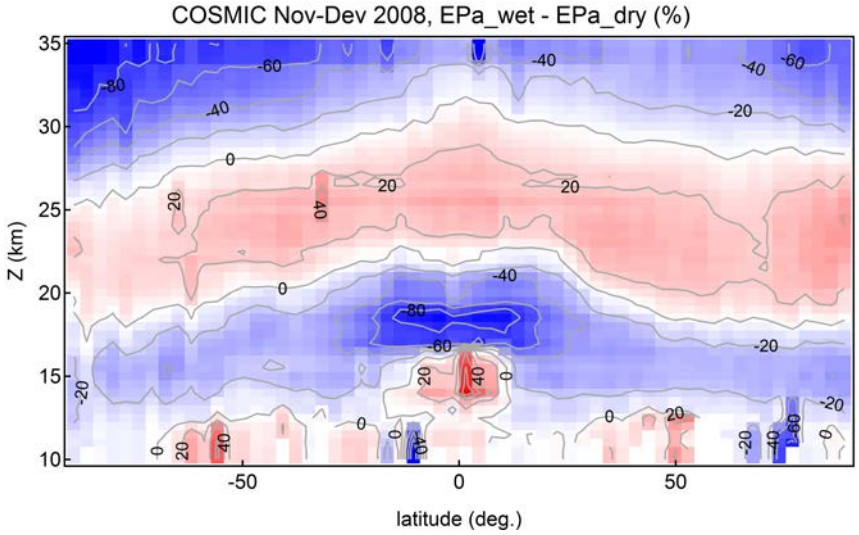

Figure 8. Latitude-altitude dependence of the zonal-mean relative difference between GW potential energy derived from wet and dry temperature and pressure profiles.

3.2 Computation of GW parameters

3.2.1 Existing methods

As discussed in Sect. 2.2, RO technique, featuring numerous advantages for the detection of GWs, has a number of limitations, arising primarily from the observation geometry. A common problem linked with GW detection using any type of observations is the determination of the background atmospheric state, i.e. the detrending of large-scale processes from the measured temperature profile. According to the linear theory of GW [Fritts and Alexander, 2003], the measured temperature profile T(z) is expanded into a background temperature $\overline{T}(z)$ and a perturbation *T'(z)*, which can be considered as fluctuation:

$$T'(z) = T(z) - \overline{T}(z). \qquad (10)$$

The background is assumed to be steady, the fluctuations are much smaller than the background and do not affect the former. Usually, *T'* is assumed to be due entirely to GWs, although the correctness of this assumption strongly depends on the approach to background separation. The choice of the background state significantly affects the results and it is quite a complicated issue, because a model can never perfectly reflect the real state of the atmosphere.

There exists various methods for determination of the background state based essentially on horizontal and vertical detrending, each of which having its own limitations. The most commonly used methods are:

1) Band-pass filtering with cutoffs at specific vertical wavelengths applied directly to the temperature profile [Steiner and Kirchengast, 2000; Tsuda et al., 2000; Schmidt et al., 2008). The resulting T' profiles in this case may still include large-scale waves and be affected by the tropopause variability.

2) Low-order polynomial fitting of the temperature profile, possibly combined with high-pass filtering of the resulting perturbation profile [Wang and Geller, 2003; Gubenko et al., 2012; Khaykin et al., 2015]. Depending on the order of polynomial chosen, several harmonics of the waves will be suppressed, hence the method is subjective to the order used. This method may also be affected by vertical structures in the tropopause layer, which may be aliased as GW perturbations.

3) Computation of background profile for a fixed spatiotemporal grid (e.g. 20° longitude × 5° latitude × 7 days) followed by low and high pass filtering of the background and perturbation profiles respectively [S.P. Alexander et al., 2008a,b; Khaykin et al., 2015]. This method efficiently removes most global-scale waves with large horizontal wavelengths, however some contribution from high phase speed Kelvin waves may remain.

4) Estimation of amplitudes and phases of zonal wavenumbers 0-6 using S-transform to define the large-scale temperature variation, which is then subtracted from individual profiles or clusters of profiles [Wang and Alexander, 2010; Faber et al., 2013; Schmidt et al., 2016]. This method requires high sampling density and therefore can not be applied to the entire GW period. Also, in this method, spatial structures with zonal wavenumber > 6 may leak into the estimated GW field.

The methods 1 and 2 can be classified as vertical detrending methods, which can be applied to any type of data set (e.g. lidar, radiosondes) whereas 3 and 4 are essentially horizontal detrending methods, requiring a global data set, i.e. satellite observations or model reanalysis. Depending on the method applied, the resulting quantities describing GW activity would be biased either by missing a certain range of GW spectrum (which is also related to the measurement geometry in the case of RO) or due to aliasing the global-scale waves (e.g. Rossby or Kelvin waves) as GWs.

John and Kumar [2013] compared the GW potential energy computed from COSMIC and SABER data using methods 1 and 4 and found significant differences in the magnitude of potential energy. Schmidt et al. [2016] used triplets of COSMIC and CHAMP RO data to estimate GW potential energy and momentum flux using methods 1 and 4 and found that vertical detrending yields higher E_p values in the tropics (compared to the results of horizontal detrending) and lower values at the southern midlatitudes. The same conclusions were reached for the momentum flux. In addition, the authors demonstrated that horizontal detrending approach, where ERA-Interim reanalysis was used

to derive the background state profile yields GW parameters, were consistent with those obtained by observation-based horizontal detrending.

Many authors have noted that any method overestimates E_p in the lowermost stratosphere by aliasing the non-linear gradient background temperature profile near the tropopause, which leads to artificial enhancement in the wave activity. Schmidt et al. (2012) suggested two possible approaches to solve this problem: a separation of the profile into tropospheric and stratospheric parts and application of a filter for each region. Sacha et al. [2014] proposed to use RO density profiles for GW analysis and argued that using density instead of temperature profiles bears certain advantages.

3.2.2 Applied methods

For constructing the experimental ROMSAF GW product two methods were applied – method 2, which represents a pure vertical detrending and method 3, which is essentially a horizontal detrending method with additional spectral filtering to select the desired spectrum range of vertical wavelengths.

Before computation of GW parameters ROM SAF dry temperature and refractivity were interpolated to a fixed vertical grid ranging from 10 to 35 km with a vertical step of 500 m, which is somewhat an oversampling for RO data in the stratosphere. The dry pressure was calculated from refractivity using Eq. 9. The essential steps leading to estimation of potential energy using vertical and horizontal detrending methods are illustrated in Figure 9 and described below.

Vertical detrending

1. Determination of background state temperature profile $\overline{T}(z)$ (solid black curve in Fig. 9a) by polynomial fitting (6^{th} order) of each individual dry temperature profile (red curve in Fig. 9a).
2. Extraction of temperature perturbation profile $T'(z)$ using Eq. 10.
3. Welch-windowing of temperature perturbation profile (to reduce spectral leakage)
4. High-pass filtering of the resulting perturbation profile with a cut-off at 7 km (solid black curve in Fig. 9b) or 13 km depending on the desired range of vertical wavelength spectrum.
5. Calculation of vertical profile of potential energy per unit of mass, E_p (solid black curve in Fig. 9c) using Eq. 7, where Brunt-Vaisala frequency squared (N^2) is smoothed using binomial (Gaussian) smoothing of 10^{th} order.
6. The obtained potential energy profile is vertically averaged over 7 km.

Horizontal detrending

1. Determination of background state temperature profile $\overline{T}$ (z) and N^2 by averaging all individual temperature profiles in a grid box 20° longitude × 5° latitude × 7 days.
2. Low-pass filtering of the background profile with a cut-off at 7 (13) km to remove the possible remaining perturbations due to GWs (dashed black curve in Fig. 9a).
3. Extraction of temperature perturbation profile $T'(z)$ using Eq. 10.
4. Welch-windowing of temperature perturbation profile

5. High-pass filtering of the resulting perturbation profile with a cut-off at 7 km (dashed black curve in Fig. 9b) or 13 km depending on the desired range of vertical wavelength spectrum.
6. Calculation of vertical profile of potential energy per unit of mass, E_p (dashed black curve in Fig. 9c) using Eq. 7.
7. The obtained potential energy profile is vertically averaged over 7 km.

The two methods differ only in the determination of the background state. As can be inferred from Fig. 9, despite the fact that the background profile obtained by horizontal detrending method may be very different from the individual polynomial fitting, the resulting perturbation and potential energy profiles are very similar. This is due essentially to the high-pass filtering, which effectively removes any vertical trend or bias between the individual and background profiles.

The computation of E_p was performed for the entire ROM SAF CDR using both detrending methods. For each of the methods E_p was estimated for GW with short vertical wavelengths 2 km < λ_z < 7 km, E_{p7} and the entire spectrum of wavelengths, which can be resolved by RO technique: 2 km< λ_z < 13 km, E_{p13}.

The vertical wavelength was calculated by performing Fourier transform to each individual temperature perturbation profile (computed using horizontal detrending method) and determining the dominant and second-order wave numbers.

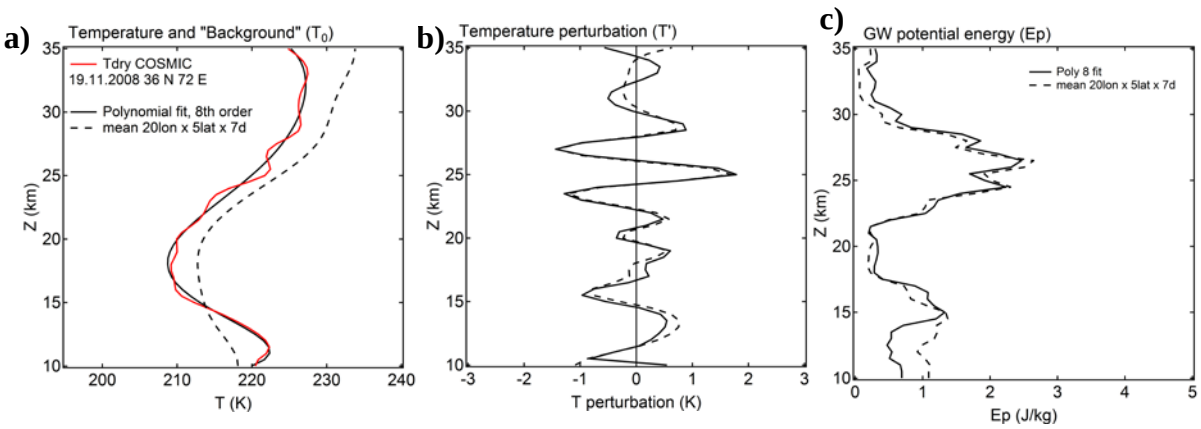

Figure 9. Essential steps in computation of GW potential energy vertical profile using vertical and horizontal detrending: individual and background temperature (a); temperature perturbation (b) and potential energy (c) vertical profiles. See text for detail.

An important consideration relevant to the horizontal detrending method applied to available RO data is the number of temperature profiles in the spatiotemporal grid box used for determination of the background state profile. Fig. 10 shows the temporal evolution of sampling density (number of profiles per grid) over the time span of ROM SAF data set for the 50° N latitude (where sampling is highest) and equator (where sampling is three times as low according to Fig. 4). The plot in Fig. 10 shows that before 2006, when CHAMP was the only operational RO mission, the sampling density does not exceed 3 profiles per grid box for 50° N and remains at or below 2 profiles at the equator. Under such conditions, when the number of profiles per grid approached unity, the horizontal detrending becomes

essentially a vertical one as the background profile is then obtained from low-pass filtering applied to the individual temperature profile.

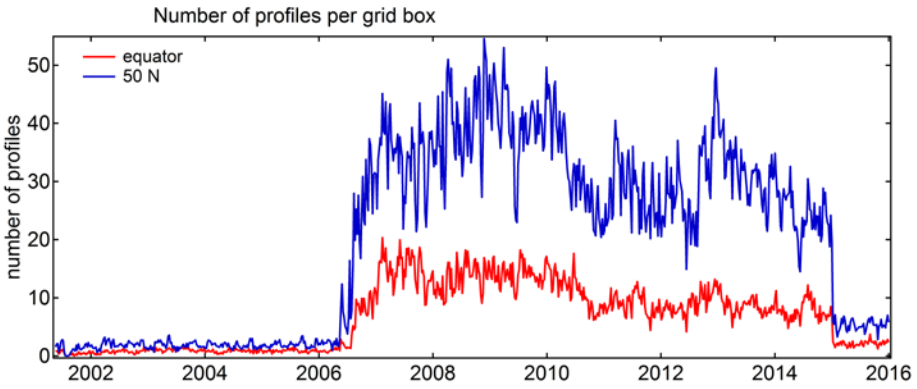

Figure 10. Time series of zonal-mean sampling density (number of profiles per spatiotemporal grid box 20° longitude × 5° latitude × 7 days) at midlatitudes and at equator.

3.2.3 Comparison of results obtained using different methods

As pointed out above, the detrending methods have their particular limitations and may lead to significant differences in the resulting fields of GW parameters, particularly the potential energy. When a global data set is available, as is the case for RO observations, the horizontal detrending method is preferred because the background state profile is better representative of the actual unperturbed state of the atmosphere than the polynomial fitting and/or high pass filtering applied to a single profile. At the same time, the horizontal detrending, which includes temporal averaging, could remove some quasi-stationary waves that may be better captured by the vertical detrending method [Alexander et al., 2008a]. Also, the vertical detrending is better compatible with the GW analysis performed using local observations (e.g. lidars or radiosondes) [Khaykin et al., 2015], which are restricted to the use of vertical detrending.

The effect of the application of different methods on the resulting potential energy fields is displayed in Fig. 11, which compares geographical distributions of E_{p13} during boreal summer obtained using horizontal, (Fig. 11a) and vertical (Fig. 11b) detrending methods, E_{p13HD} and E_{p13VD} respectively. Fig. 11c shows the relative difference between the two. The pattern of difference reveals three distinct bands: northern midlatitudes, where the difference is minimal; tropics, where vertical detrending yields significantly higher E_{p13} values (reaching above 100%); and southern mid/high latitudes, where vertical detrending results in lower E_{p13} values. Fig.11d displays the dominant vertical wavelength distribution for the same season, which helps understanding the differences between the E_{p13} estimated using different methods.

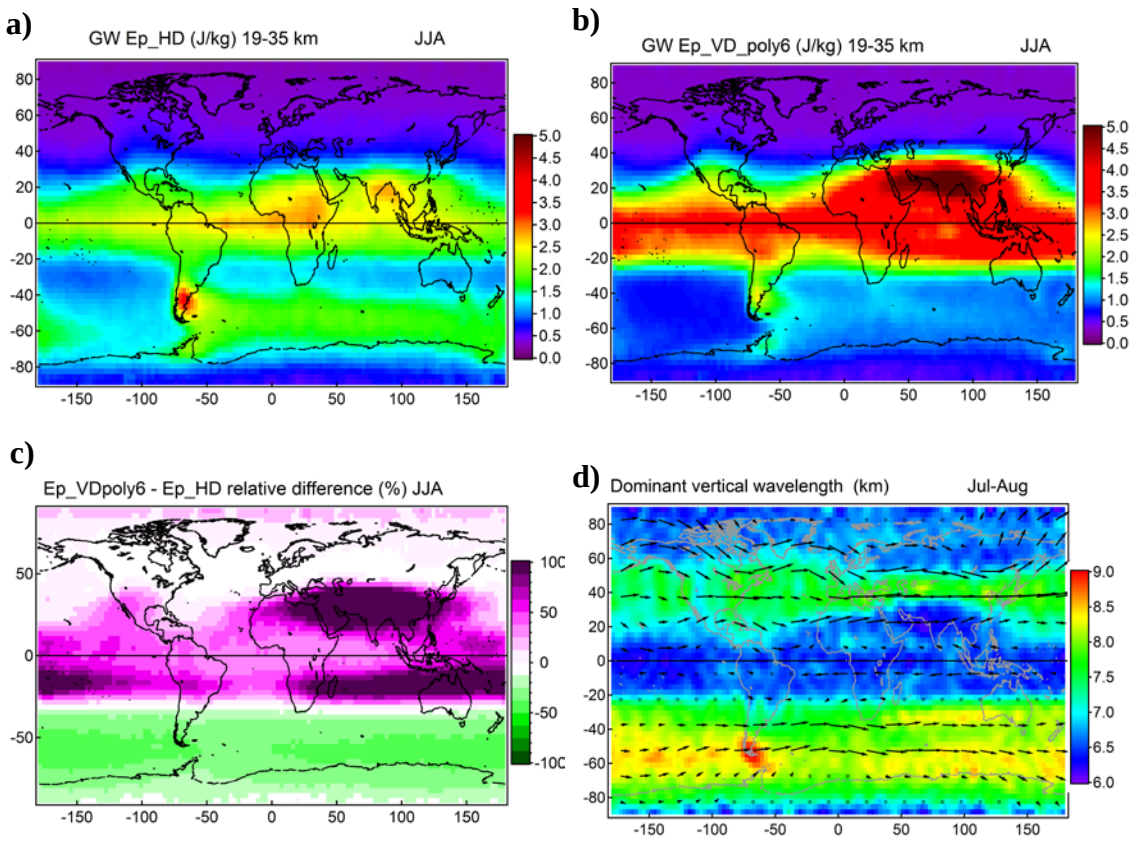

Figure 11. Geographical distribution of middle stratospheric mean (19-35 km) Boreal summer (June, July, August) a) GW potential energy computed using horizontal detrending method, E_{p13HD}; b) GW potential energy computed using vertical detrending method, E_{p13VD}; c) relative difference 100*(E_{p13VD} - E_{p13VD})/ E_{p13VD}; d) dominant vertical wavelength λ_z and wind field from ERA-Interim reanalysis.

Comparing Fig. 11c and d one can see that the regions, characterized by GWs with shorter vertical wavelengths, λ_z < 7 km (tropical belt and particularly Asian summer monsoon region – i.e. convective regions) correspond to the positive bias between E_{p13VD} and E_{p13HD}. Meanwhile, the negative bias is observed at southern midlatitudes, a region of longer vertical wavelengths (λ_z > 7 km). This suggests that vertical detrending method is more sensitive to shorter wavelength GWs observed in the tropical region and associated with convectively-generated GWs. Indeed, E_{p13VD} shows a maximum above the Asian monsoon region, characterized by strong convection during boreal summer season. It is also conceivable that with the vertical detrending a part of large-scale waves is still present in the temperature fluctuation and not assigned to the background [Schmidt et al., 2016].

The horizontal detrending is in turn more sensitive to GWs with longer vertical wavelength, which are observed around the northern and southern jets, where Doppler shifting of GWs in a strong background winds (shown as black arrows in Fig. 10d) renders higher vertical wavelengths. The maximum λ_z are observed above the southern tip of South America – a well known hot spot of orographic GW activity. Despite the prominent λ_z positive anomaly above this region, the difference pattern in Fig. 10c does not reveal any specific behaviour of the bias between E_{p13VD} and E_{p13HD} above this region. This suggests

that the bias is less dependent on λ_z in the longer wavelength range. Importantly, the minimum E_{p13VD} - E_{p13HD} bias is observed above the northern extra-tropical region, where E_{p13} obtains very low values (<1 J/kg) during boreal summer and λ_z remains in the 7 – 8 km range.

In summary, the vertical detrending using the 6th order polynomial fitting yields higher E_{p13} values for the convectively generated GWs characterized by short vertical wavelength, whereas horizontal detrending yields higher E_{p13} values for the longer λ_z, associated with the Doppler shifting of both orographic and non-orographic GWs. The detrending methods agree well in capturing the summer hemisphere minimum of GW activity at midlatitudes. Similar behaviour of the bias pattern is observed in other seasons (not shown).

3.3 Results: climatology of GW parameters (E_p and λ_z)

The results of ROM SAF data analysis include the following output data sets (stored as HDF5 files), of which the vertically-resolved data cover 10..35 km altitude range with 0.5 km vertical step:

1) GW potential energy vertical profiles calculated using horizontal detrending method for the vertical wavelength range 2 km < λ_z < 7 km, E_{p7HD}
2) GW potential energy vertical profiles calculated using horizontal detrending method for the vertical wavelength range 2 km < λ_z < 13 km, E_{p13HD}
3) GW potential energy vertical profiles calculated using vertical detrending method for the vertical wavelength range 2 km < λ_z < 7 km, E_{p7VD}
4) GW potential energy profiles calculated using vertical detrending method for the vertical wavelength range 2 km < λ_z < 13 km, E_{p13VD}
5) Dominant and secondary vertical wavelength of GW calculated using horizontal detrending method, λ_z

Figure 12 provides the climatological (based on the entire ROM SAF CDR) geographical distribution of E_{p7HD} for different seasons. E_{p7HD} is averaged between 19 and 35 km. The lower boundary of vertical range for averaging is chosen to exclude the tropopause layer (extending up to 18 km in the deep tropics), in which strong temperature gradients and high tropopause variability may result in overestimation of GW activity (see Sect. 3.2.1).

The general pattern of GW activity reveals a maximum around the equator during all seasons, a minimum at midlatitudes during local summer and enhanced GW activity during local winter occurring mainly above the continents or, more specifically above the areas with high topography. In the Northern hemisphere the source regions of orographic GW generation are Rockies, Scandinavian mountains, Tian Shan etc.), whereas in the Southern hemisphere the most prominent orographic GW hotspots are the Andes (particularly their southern part) and Antarctic peninsula. A strong jet above the mid- and high-latitudes induces orographic generation of GWs, which can propagate freely into the stratosphere in a non-zero background wind. In the tropics the GW activity maximizes above the regions, characterized by most vigorous deep convection that is the maritime continent, equatorial Africa, Amazonian region during early Austral summer (November-December), northern equatorial Africa and Indian subcontinent during Boreal summer (July-August). The

manifestation of convectively-generated GWs can also be observed above the Indian and western Pacific oceans (November through June) and above Atlantic ocean (May through October).

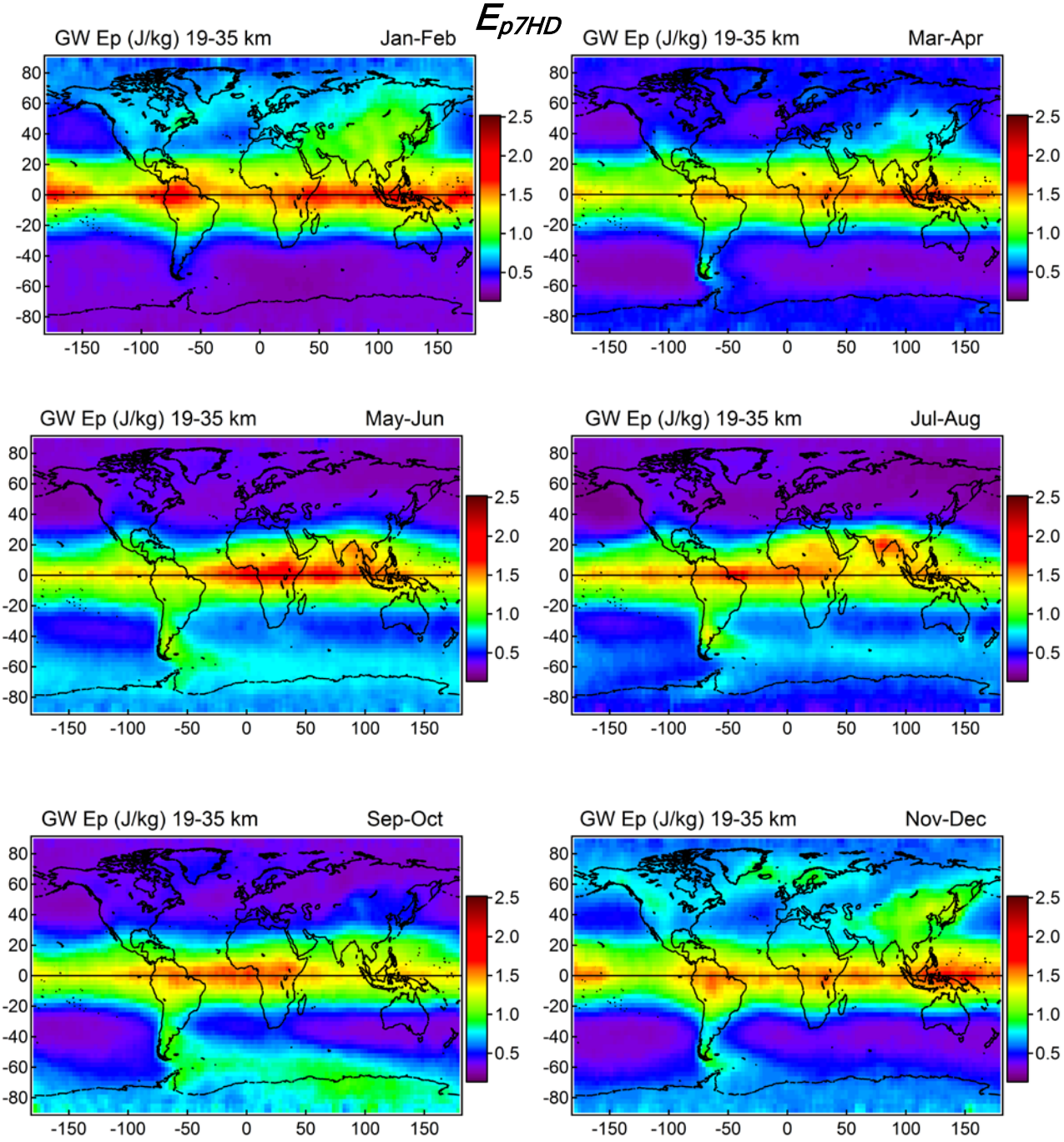

Figure 12. Geographical distribution and seasonal cycle of GW potential energy, E_{p7HD}, (averaged between 19 and 35 km altitude**)** obtained using horizontal detrending method for vertical wavelengths λ_z < 7 km.

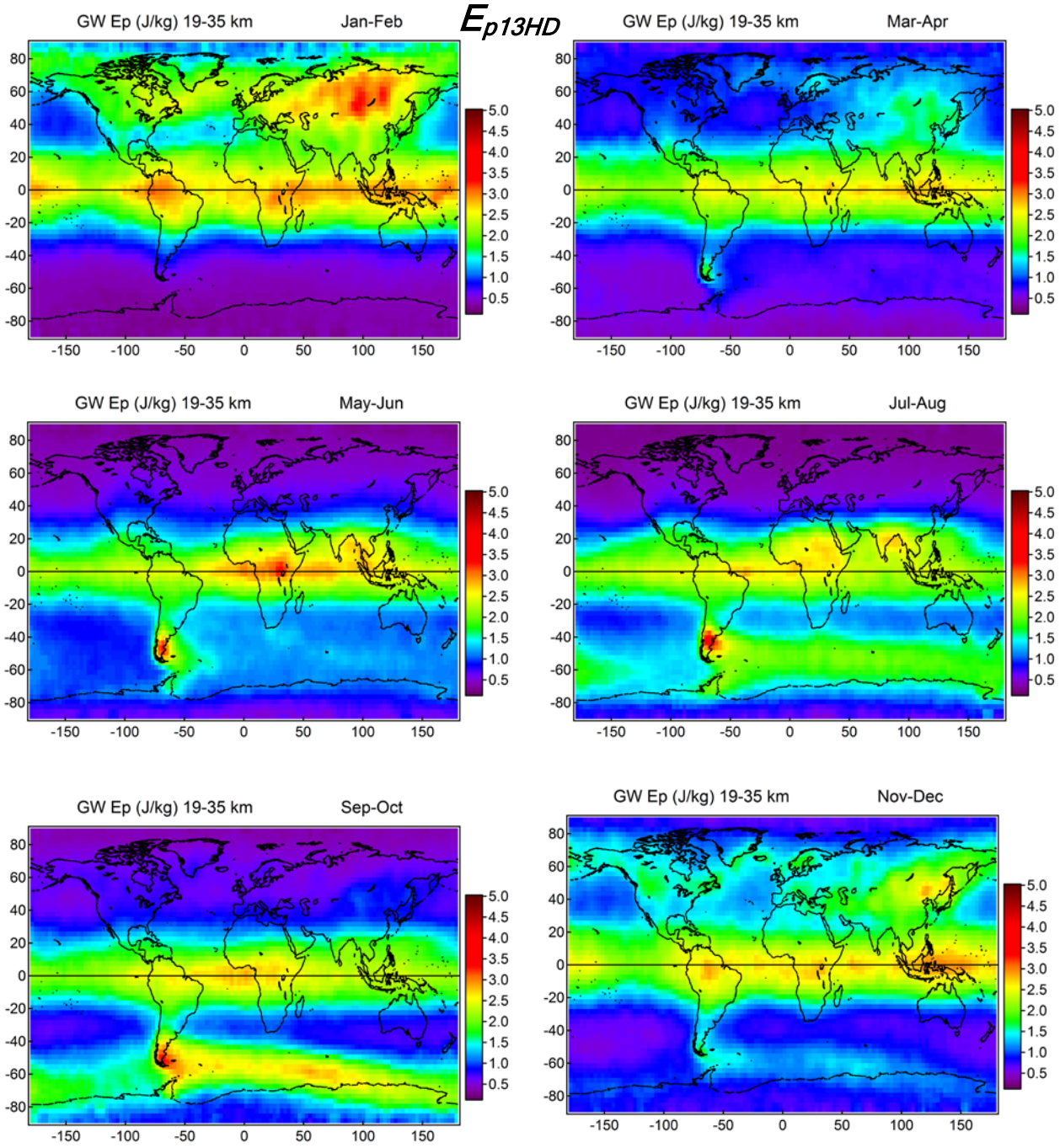

Figure 13. Geographical distribution and seasonal cycle of GW potential energy, E_{p7HD} (averaged between 19 and 35 km altitude**)** obtained using horizontal detrending method for vertical wavelengths λ_z < 13 km. Note the different color scale compared to Fig. 12.

Figure 13 displays the climatology of E_{p13HD}, which represents the GW activity for the entire spectrum of vertical wavelengths that can be observed with RO technique. Note that the color scale in Fig. 13 is twice as large as that in Fig. 12. The most remarkable

differences in E_{p13HD} geographical distribution compared to E_{p7HD} are: i) a prominent enhancement of GW activity above northern Asia during Boreal winter; ii) stronger confinement of enhanced GW activity to continents in the tropical belt during convective seasons and iii) higher intensity of the orographic GW hotspot above southern Andes. Overall, while the E_{p7HD} features an all-season maximum around the equator, E_{p13HD} exhibits two pronounced maxima located above Northern Asia and southern Andes.

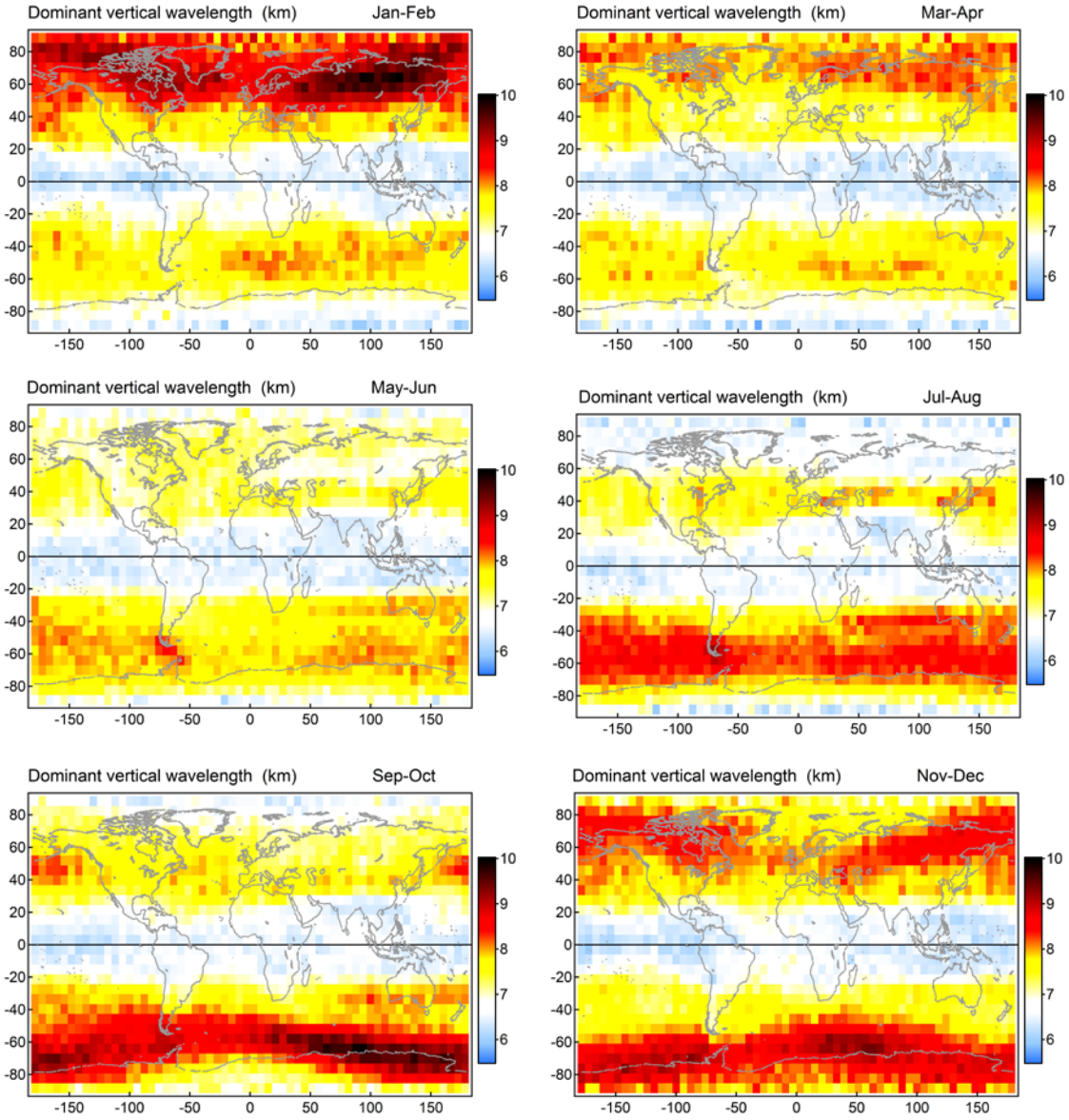

Figure 14. Geographical distribution and seasonal cycle of dominant vertical wavelength λ_z.

The observed differences between E_{p7HD} and E_{p13HD} are better understood under consideration of the dominant vertical wavelength and its geographical variation as a function of season. The climatology of λ_z is provided in Fig. 14, which reveals the following features: i) dominant λ_z is bounded between 5 and 10 km; ii) the maximum

values of λ_z are observed at high latitudes during local winter and mostly coincide with the enhancements in E_{p13HD} (e.g. northern Asia and southern Andes); iii) smaller λ_z values are observed in the tropical belt and at high latitudes during local summer; iv) the lowest vertical wavelengths (λ_z < 6 km) correspond to the areas of strongest convection (e.g. Indian subcontinent during Boreal summer and maritime continent during Austral summer). Based on the above one can infer the following i) convectively-generated GWs feature shorter dominant wavelengths (λ_z < 7 km); ii) strong zonal winds occurring within the polar jets and vortices are responsible for the Doppler-shifting of GWs to higher λ_z; iii) orographic GWs can be characterized by longer λ_z.

Considering the range of estimated λ_z, one can conclude that E_{p7} - containing only the short-wavelength GWs – misses an important part of the GW spectrum accessible with RO technique. On the other hand, the planetary-scale waves as Kelvin and Rossby waves, characterized by longer λ_z [e.g. Alexander et al., 2008b] are more likely to leak into E_{p13} and result in overestimation of the GW energy.

The E_p fields described above represent an average over the middle stratosphere – 19 .. 35 km. In order to investigate the vertical distribution of stratospheric GW potential energy and its annual cycle, Fig. 15 provides the month-altitude sections of E_{p7HD} for 6 different latitude bands. At high latitudes, GW activity is mainly restricted to local winter and altitudes above about 20 km. In the Arctic, GW activity peaks in mid-winter (late January), whereas in the Antarctic region such maximum occurs in Spring (October). Both Arctic and Antarctic GW activities exhibits a maximum above 31 km occurring during fall season; this maximum is stronger pronounced in Antarctic region. In the lower layers (z<15 km), GW activity maximizes during local summer at both hemispheres, whereas the late winter maximum is exclusive to Antarctic region.

The annual cycle of GW E_p vertical distribution at high latitudes and the differences between the Arctic and Antarctic regions can largely be explained by considering the dynamics of polar vortices, the annual cycle of wind velocity and wind shear as well as by the topography. In this way, the stronger and more stable Antarctic polar vortex can be contrasted to a highly variable Arctic vortex, which often becomes perturbed by the so called Sudden Stratospheric Warming (SSW) events. SSWs are triggered by the planetary wave activity in the Northern hemisphere leading to major perturbation of the vortex, accompanied by the outbreaks of GW activity [Hei et al., 2008; Wang and Alexander, 2009; Mze et al., 2014]. Note though that the SSW events in the Arctic may occur at any time between December and March, whereas the results provided here are based on the data spanning 14 years. Nevertheless, January-February is the season when SSW events are most likely to occur [Maury et al., 2016], which may explain the late January peak in GW activity in the Arctic. SSW events are, in turn, very rare in the Antarctic and the mid-stratosphere peak in October is rather related to the breakdown of the strong Antarctic vortex in Austral spring. Another factor responsible for the Arctic versus Antarctic differences is the large contribution from the orographic GW hot spots in southern Andes and Antarctic Peninsula.

At the northern mid-latitudes GW activity exhibits a minimum at all levels during local summer, a maximum between 20-26 km during winter and a strong maximum in the lowermost stratosphere during spring. A similar seasonal pattern with the mid-stratosphere winter maximum can be inferred for the southern mid-latitude, however there the lowermost stratosphere E_p maximum occurs in fall. Another common feature in the northern and southern midlatitudes GW annual cycle is the uppermost layer winter

maximum occurring above 30 km, seemingly separated from the mid-stratosphere E_p maximum. The major factor determining to the midlatitude GW activity and its annual cycle are [Khaykin et al., 2015]: i) orographic GWs and their propagation to the stratosphere, depending on the wind speed and directional shear; ii) stratospheric generation of GWs related to instabilities of the stratospheric jet stream (geostrophic adjustment).

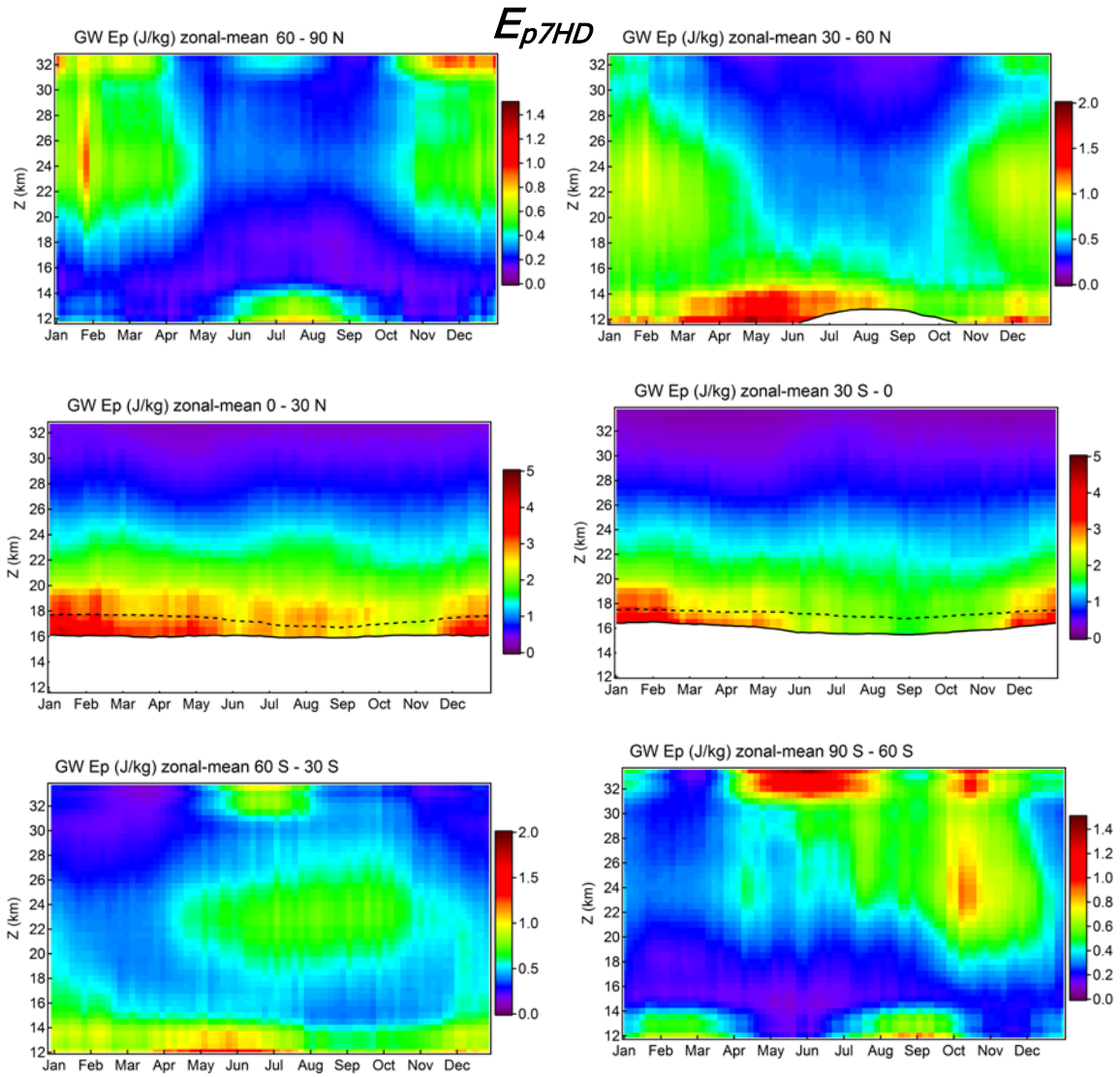

Figure 15. Month-altitude sections of zonal-mean E_{p7HD} for different latitude bands. Solid and dashes curves indicate the lapse rate and cold point tropopause levels respectively. Data below the lapse rate tropopause are not shown.

In the tropics, the zonally-averaged annual cycle for both Northern and Southern hemispheres shows a maximum of GW activity in the lower stratosphere and very low potential energies (E_{p7HD} <1 J/kg) above 24 km. While both northern and southern tropics share the annual maximum of GW activity during Austral summer, the northern tropics are

characterized by higher E_{p7HD} during Boreal summer, which appears to be a contribution from the convection within the Asian monsoon, responsible for the regional maximum of GW activity as inferred from Fig. 12. Overall, the GW activity in the tropical region is largely driven by geographical distribution and the annual cycle of deep convection with the main contributors being the Maritime continent convection (maximizing in Austral summer) and the land convection (particularly within the summer monsoons) during Boreal summer.

Of crucial importance for the tropical GW activity is the quasi-biennnial oscillation (QBO), which is strongly coupled with the gravity waves (see Sect. 1.2). Figure 16 provides an insight into this phenomenon by showing the equatorial time series of E_{p7HD} vertical distribution in the 19 – 34 km altitude range. The GW activity in the equatorial band reveals a periodic pattern, characterized by downward propagating enhancements, occurring with a quasi-biennial period. This pattern is strongly correlated with the QBO-induced variation of zonal wind speed and direction [e.g. Alexander et al., 2008b]. While such behaviour of equatorial stratosphere GW is expectable, an important inference that can be made on the base of Fig. 15 is that the QBO-related pattern of E_{p7HD} is captured equally well by the CHAMP observations, in which the sampling density is an order of magnitude smaller than that of the post-2006 RO observations.

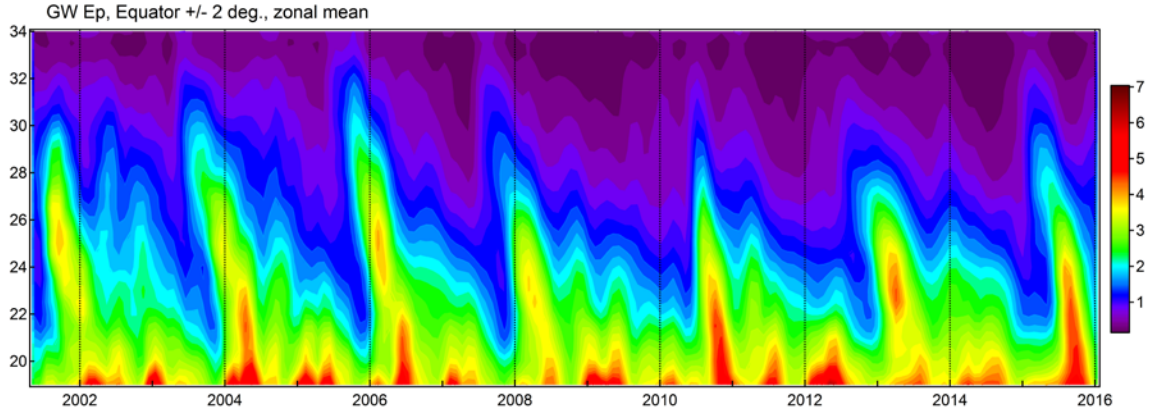

Figure 16. Time series of zonal-mean E_{p7HD} vertical distribution at the equator (+/- 2 deg.)

3.3.1 Comparison with state-of-the-art

There exist a number of studies providing global or zonally-restricted information on GW parameters, most of them are cited in Sect. 2.2. The most commonly reported parameter is the potential energy, which serves a convenient proxy for GW activity. Fewer studies provide information on vertical and horizontal wavelengths and GW momentum flux. The results of E_p and λ_z estimation on the base of ROM SAF V.0 data set, although covering a much longer time period than usually exploited in the literature, can be compared with the previous studies.

The magnitude, distribution and variability of E_{p7HD} can be compared with the results provided by Alexander et al., [2008a] and [2008b], who used horizontal detrending method (very similar to the one applied here) for computing potential energy of GW with $\lambda_z < 7$ km. Alexander et al., [2008a] found E_{p7HD} values for the Northern hemisphere winter ranging from 0.2 to 2.8 J/kg, which is fully consistent with our results. Alexander et al.,

[2008b] investigated E_{p7HD} variability in the tropics and found a QBO-related signal in E_{p7HD} with the values ranging between 0.5 and 5 J/kg above 20 km. This is in close agreement with the results provided in Fig. 16.

Sacha et al. [2015] used COSMIC density profiles instead of temperature to compute global distribution of GW potential energy and found a hotspot above Northern Asia, which we noted in Fig. 13. de la Torre et al., [2006] analyzed 5 years of CHAMP data using vertical detrending method with different cut-off wavelengths and found E_{pVD} values, which are in agreement with our analysis. Faber et al. [2013] used horizontal detrending method (in a somewhat different way than here) to derive GW parameters and reported global distribution of E_{pHD} Boreal and Austral summer seasons, with which our results are fully consistent except that the magnitudes of potential energy reported are about 30% higher than those of our analysis. At the same time, the magnitude of λ_z and its latitude distribution in our analysis are fully compatible with Faber et al., [2013]. Our λ_z estimates also agree reasonably well with Wang and Alexander [2008].

Schmidt et al. [2016] estimated GW potential energy and vertical wavelength among other parameters using horizontal and vertical detrending methods. The results of our analysis, particularly the latitude distribution of E_{p13HD} and λ_z, are fully consistent with their estimates. In addition, Schmidt et al. [2016] found higher (lower) potential energies in the tropics (southern mid-latitudes) using vertical detrending method – a conclusion that was reached on the base of our analysis (Figure 11).

Overall, the results provided here are fully compatible with the literature despite a large diversity of methods exploited and temporal periods analyzed.

3.4 Gridding options and statistical error

As pointed out in Sect. 3.1.1, the sampling density of the RO observations during the CHAMP era (i.e. before 2006) is an order of magnitude lower than that of the observations after 2006, when COSMIC and other RO missions were placed into orbit. In this Section we consider different gridding options for the end-user GW product and discuss the associated statistical errors.

The climatology of GW parameters in Sect. 3.3 is reported with a horizontal resolution 3°×3°, which enables to resolve small-scale GW features associated with orographic or convective generation. At 5° × 5° resolution the small-scale features are still discernible, however a further enlargement of the spatial grid may smear important signals of GW activity. As for the temporal resolution, while the GW activity is variable on the weekly scale due to e.g. thunderstorms or wind flow perturbations [Khaykin et al., 2015], the 1-week grid cells may not provide sufficient sampling for the CHAMP era.

Figure 17 shows time-latitude variation of the zonally-averaged number of RO profiles per spatiotemporal grid for various grid sizes. The plots display only those data points, where the zonal-mean number of profiles per grid exceeds 1. That is to say, the blank areas in the plots indicate that for a given latitude band the number of empty grid cells exceeds the number of cells containing at least 1 profile.

Figure 17a suggests that at 3°×3°×1 week resolution, the sufficient sampling is achieved only during 2007-2009 time period, when COSMIC mission was in good health and providing up to 2000 occultations per day. Using 5°×5°×1 week resolution (Fig. 17b) significantly improves the picture, rendering the entire COSMIC period sufficiently sampled with global coverage. The CHAMP period is, however, still strongly

undersampled with this resolution. If the temporal gridding is increased to 1 month, the spatial resolution of 5°× 5° ensures a sufficient sampling for the CHAMP period (Fig. 17c, note the different color scale).

Figure 18 provides an insight into statistical errors associated with different spatiotemporal resolutions. The standard error was obtained by computing the standard deviation of the vertically averaged (19..35 km) E_{p13HD} values in a grid cell of a given size and dividing it by the square root of the number of profiles in this grid. The standard errors were then zonally averaged for each latitude belt to obtain a latitude dependence of the error. The error resulting from the 5°× 5°×1 week resolution for the COSMIC era (black curve) amount to about 20% at midlatitudes, while increasing towards the poles. The error becomes noticeably larger for the same time period if the spatial grid is reduced to 3°× 3° (red curve). The monthly 5°× 5° gridding results in a low statistical error for the COSMIC period (violet curve), which becomes 2.5 times higher for the CHAMP period.

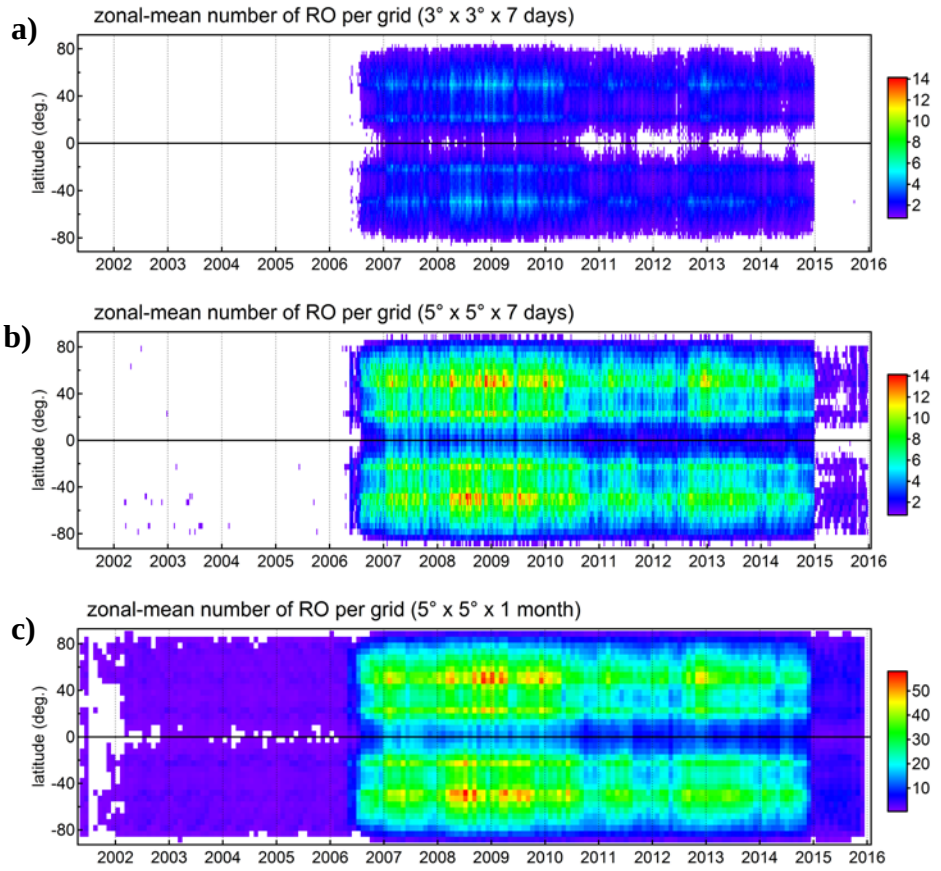

Figure 17. Time-latitude variation of the zonally-averaged number of RO profiles per spatiotemporal grid for various grid sizes. Only the data points, where the zonal-mean number of profiles per grid exceeds 1 are shown.

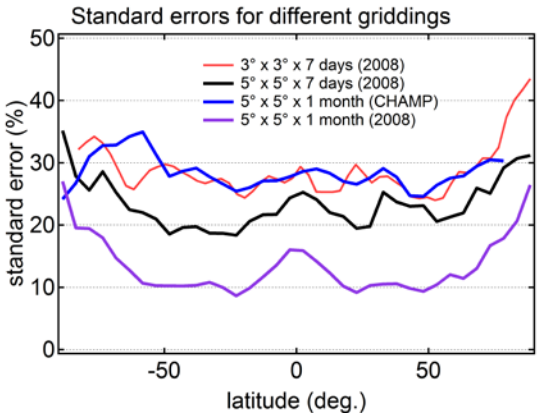

Figure 18. Zonally-averaged standard (statistical) errors of E_{p13HD} for different grid sizes and time periods as a function of latitude.

In summary, during the COSMIC era a resolution of 5°×5°×1 week ensures a sufficient sampling and moderate statistical errors, whereas for CHAMP, a monthly averaging is required.

4. Recommendations for future ROM SAF data and GW products

This chapter provides a set of recommendations for the future ROM SAF data products relevant for GW studies. Such product can be demanded by the atmospheric scientists focusing on stratospheric dynamics and climate modelers wishing to validate their model simulations using the observational data. The recommendations are based on the outcome of the present feasibility study and the common knowledge available in the literature. Two sets of recommendations are provided: for L2 dry temperature profiles and for L3 gridded GW parameters.

As follows from the literature overview, RO-based data on dry temperature have been used by many authors for retrieving GW parameters. It is then possible that a user, who has already acquired an experience with RO data and/or GW analysis would opt to perform his/her own retrieval of GW parameters using the original data on dry temperature and refractivity. For this scenario, the end product could be conceived in such a way to facilitate the data handling and analysis. The present ROM SAF data set is organized such that each occultation is archived in an individual file. While this approach to RO data archiving is commonly implemented by RO processing centers, it is not optimal in terms of data manipulation. At present, the cumulative number of occultations available from different RO missions approaches 10 millions. Handling such a large number of single files is a resourceful job for any operating system. In reality, any kind of manipulation (download, transfer or reading routine) performed on a multimillion set of files may take up to several days.

Another issue concerning the current version of ROM SAF data set is an excessive number of parameters reported in the files. For a user wishing to extract GW parameters from the original data, one can restrict to a set of essential data fields required for GW analysis, which would furthermore be reported only for the vertical range, where dry temperature information is reliable. This way, the volume of data may be significantly reduced, making the data set easier to handle. Following the above considerations, the recommendations for the ROM SAF end user original product are:

R1. To group the single occultations into daily files, i.e. the files containing all occultations for a given day from all RO missions.

R2. To limit the parameters archived to those required for GW analysis, namely:

- dry temperature
- dry pressure
- coordinates of tangent point
- date and time of the observation
- lapse rate tropopause altitude, pressure and temperature

The temperature and pressure profiles can be interpolated onto a fixed altitude grid with a vertical step of 200-500 m covering the vertical range between 8 and 40 km. At that, it should be kept in mind that dry temperature becomes biased in the troposphere due

to effect of water vapour, hence the lower vertical boundary is basically constrained by the tropopause altitude and, possibly a few hundreds of meters below that level. Thus, the tropopause height is an important parameter required to restrict the GW analysis to a vertical range of reliable measurements. The recommended upper boundary of vertical profiles is set to 40 km, however the data above 35 km should be treated with caution as the vertical resolution and measurement precision degrade rapidly already above 30 km [Scherllin-Pirscher et al., 2011].

Users who are willing to avoid a manual retrieval of GW parameters can benefit from the gridded ROM SAF L3 GW products, for which the recommendation can be as follows.

R3. GW data gridding

In order to adequately describe the GW activity during CHAMP and COSMIC eras with very different sampling densities, two types of gridding are required: 5°×5°×1 week for the COSMIC time span and 5°×5°×1 month for the entire RO observation period (Sect. 3.4).

R4. GW retrieval method (background state determination)

Horizontal detrending method, in which the background state is deduced from the adjacent observations, represents a more physical way to assess the GW parameters. However, this method can not be implemented in NRT processing and requires a sufficient sampling. An alternative approach to horizontal detrending could be a use of operational analysis and forecast data provided by ECMWF for determination of the background state (sect. 3.2.1). The GW product based on vertical detrending could be produced in NRT mode and represents a certain value for comparisons with GW time series obtained from local measurements (e.g. lidars or radiosondes), which can only rely on vertical detrending.

R5. GW parameters

The parameter most widely used as a proxy for GW activity is the potential energy, E_p, which along with the vertical wavelength λ_z can in principle be deduced from a single RO profile. The GW momentum flux is another important parameter, which is necessary to estimate the level of wave breaking and hence the effect of GWs on the mean flow – a parameter highly demanded by the modelers. Determination of momentum flux (and horizontal wavelength λ_h) is more challenging as it requires a use of the triplets of nearby (<250 km) profiles taken with a short time interval shorter than 1 hour. The theoretical basis of this method and its limitations can be found in [Schmidt et al., 2016 and references therein].

R6. Other properties of GW product

As shown in Sect. 3.3, potential energy varies strongly with altitude, therefore this parameter should be reported as a vertical profile with a resolution of 2-3 km for the vertical range between the tropopause and 35 km. Higher vertical resolution is not necessary as the GW product is intended to be a gridded data set. The data on dominant vertical (horizontal) wavelength can be reported for different height intervals (with 5 or 10 km step) or for the entire stratosphere.

It is of utility to report the GW potential energy for different ranges of wavelength, e.g. for $\lambda_z < 7$ km and for $\lambda_z > 7$ km (or a full spectrum). The former is limited to a certain part of GW spectrum; however the latter is more likely to be influenced by unaccounted large-scale waves.

5. Summary

The undertaken study addresses the problematics of gravity waves (GWs) retrieval from RO measurements and projects it onto the new ROM SAF CDR V.0 yielding a set of recommendations for the future improved ROM SAF L2 and L3 products relevant for GW analysis.

The first part of the report provides the basic theory of atmospheric gravity waves, lists their essential parameters and reviews the current state of knowledge on the retrieval of GW parameters from RO measurements. The literature overview points out that RO-based GW retrieval is a subject of a number of studies since 2000 exploiting different retrieval methods and limited observation periods. The main limitations of RO-based GW retrieval are caused by the RO vertical resolution, vertical range limited to about 35 km and measurement geometry, which do not allow for detecting GWs with vertical wavelength smaller than 2 km and horizontal wavelength smaller than 100-200 km. In most cases, observation geometry relative to the GW field results in a weakening of the wave amplitudes and biased estimation of the vertical wavelengths. Despite these limitations, the RO technique, featuring high resolution and accuracy, represents a major source of information for GW analysis, which is why it is widely used for this matter.

The second part of report evaluates the ROM SAF CDR V.0 in terms of the available data fields, sampling density and its variation with time. The data set available at the time of writing includes the data from CHAMP, COSMIC, GRACE and METOP-A missions spanning 2001 through 2015 and comprising over 6 millions radio occultations. We note that the sampling frequency during the CHAMP era was an order of magnitude lower than that after the launch of COSMIC and other RO missions in 2006-2007. Intercomparison of dry and wet (1D-var) temperatures reveals important discrepancies throughout the stratospheric range of altitudes between both the temperature profiles themselves and their vertical fluctuations, which are associated with GW activity.

The overview of existing methods for GW retrieval brings out the problem of determination of the background (unperturbed) state of the atmosphere and identifies two essential approaches to the solution: horizontal and vertical detrending methods. The horizontal detrending method, requiring a global data set with sufficient sampling, represents a more physical way to determine the background state. In turn, the vertical detrending method, in which the background state is derived from polynomial fitting or band-pass filtering applied to the temperature profiles itself, is more compatible with the sparse data sets.

Comparison of the results of computation of GW potential energy using different methods shows that the vertical detrending emphasises GWs with short vertical wavelengths, prevailing in the tropical regions of deep convection, whereas the horizontal detrending emphasises the longer wavelength spectrum. It is generalized that depending on the method applied, the resulting quantities describing GW activity would be biased either due to missing a certain range of GW spectrum or due to aliasing the large-scale waves as GWs.

After a description of the analysis applied to the ROM SAF CDR V.0, we present a new 14-year climatology of the two essential GW parameters: potential energy (E_p) and dominant vertical wavelength (λ_z). The potential energy was derived for two vertical wavelength spectral ranges. The obtained geographical distribution, annual cycle and temporal variability of GW activity is interpreted under consideration of the known GW

sources (flow over orography, convection, jet stream instabilities, planetary wave activity) and GW propagation or filtering in the background flow. The distribution of the dominant vertical wavelength suggests that convectively-generated GWs are characteristic of shorter λ_z, whereas the orographic GWs have longer λ_z. The seasonal variability of λ_z points to the Doppler shifting of GWs to longer wavelengths in the subtropical and polar jets. The obtained results are fully consistent with those available in the literature.

After analysis of the statistical errors associated with different data gridding options, a set of recommendations for the future ROM SAF products is provided in Chapter 4. The experimental data set on GW parameters retrieved under this study is archived as HDF5 files.

5.1 Acknowledgments

I would like to thank Johannes K. Nielsen and Kent B. Lauritsen (DMI) for making it possible to perform this VS activity and for their support and help. I also thank Stig Syndergaard and Hans Gleisner for their interest to our findings. The discussions were always fruitful, motivating and encouraging.

6. References

Alexander, M. J., and K. H. Rosenlof (1996), Nonstationary gravity wave forcing of the stratospheric zonal mean wind, J. Geophys. Res., 101(D18), 23,465–23,474, doi:10.1029/96JD02197.

Alexander, P., et al. (2008), Interpretation of gravity wave signatures in GPS radio occultations, J. Geophys. Res., 113, D16117, doi:10.1029/2007JD009390.

Alexander, S. P., T. Tsuda, and Y. Kawatani (2008a), COSMIC GPS Observations of Northern Hemisphere winter stratospheric gravity waves and comparisons with an atmospheric general circulation model, Geophys. Res. Lett., 35, L10808, doi:10.1029/2008GL033174.

Alexander, S. P., T. Tsuda, Y. Kawatani, and M. Takahashi (2008b), Global distribution of atmospheric waves in the equatorial upper troposphere and lower stratosphere: COSMIC observations of wave mean flow interactions, J. Geophys. Res., 113, D24115, doi:10.1029/2008JD010039.

Alexander, M. J., Geller, M., McLandress, C., Polavarapu, S., Preusse, P., Sassi, F., Sato, K., Eckermann, S., Ern, M., Hertzog, A., Kawatani, Y., Pulido, M., Shaw, T. A., Sigmond, M., Vincent, R. and Watanabe, S. (2010), Recent developments in gravity-wave effects in climate models and the global distribution of gravity-wave momentum flux from observations and models. *Q.J.R. Meteorol. Soc*., 136: 1103–1124. doi: 10.1002/qj.637

Anthes, R. A., et al. (2008), The COSMIC/FORMSAT-3 mission early results, Bull. Am. Meteorol. Soc., 89(3), 313– 333, doi:10.1175/BAMS-89-3-313.

Danzer, J., Healy, S. B., and Culverwell, I. D.: A simulation study with a new residual ionospheric error model for GPS radio occultation climatologies, Atmos. Meas. Tech., 8, 3395-3404, doi:10.5194/amt-8-3395-2015, 2015.

de la Torre, A., T. Schmidt, and J. Wickert (2006a), A global analysis of wave potential energy in the lower stratosphere derived from 5 years of GPS radio occultation data with CHAMP, Geophys. Res. Lett., 33, L24809, doi:10.1029/2006GL027696.

Ern, M., and P. Preusse (2009), Quantification of the contribution of equatorial Kelvin waves to the QBO wind reversal in the stratosphere, Geophys. Res. Lett., 36, L21801, doi:10.1029/2009GL040493.

Faber, A., et al. (2013), On the determination of gravity wave momentum flux from GPS radio occultation data, Atmos. Meas. Tech., 6, 3169–3180, doi:10.5194/amt-6-3169-2013.

Foelsche, U., Borsche, M., Steiner, A. K., Gobiet, A., Pirscher, B., Kirchengast, G., and Schmidt, T.: Observing upper troposphere– lower stratosphere climate with radio occultation data from the CHAMP satellite, Clim. Dynam., 31, 49–65, 2008.

Fritts, D. C., and M. J. Alexander (2003), Gravity wave dynamics and effects in the middle atmosphere, Rev. Geophys., 41(1), 1003, doi:10.1029/2001RG000106.

Gage,K . S., andG . D. Nastrom,O n the spectrumo f atmospheric Velocity fluctuations seen by MST/ST radar and their interpretation, Radio Sci., 20, 1339-1347, 1985

Garcia, R. R., and B. A. Boville (1994), “Downward control” of the mean meridional circulation and temperature distribution of the polar winter stratosphere, J. Atmos. Sci., 51, 2238–2245.

Geller, M. et al. (2013), A comparison between gravity wave momentum fluxes in observations and climate models, J. Clim., 26, 6383–6405, doi:10.1175/JCLI-D-12-00545.1.

Gubenko, V. N., Pavelyev, A. G., Salimzyanov, R. R., and Andreev, V. E.: A method for determination of internal gravity wave parameters from a vertical temperature or density profile measurement in the Earth's atmosphere, Cosmic Res., 50, 21–31, doi:10.1134/S0010952512010029, 2012.

Hei, H., T. Tsuda, and T. Hirooka (2008), Characteristics of atmospheric gravity wave activity in the polar regions revealed by GPS radio occultation data with CHAMP, J. Geophys. Res., 113, D04107, doi:10.1029/2007JD008938.

Holton, J. R. (1992), An Introduction to Dynamic Meteorology, 3rd ed., Academic Press, London.

John, S. R., and K. K. Kumar (2013), A discussion on the methods of extracting gravity wave perturbations from space-based measurements, Geophys. Res. Lett., 40, 2406–2410, doi:10.1002/grl.50451.

Khaykin, S. M., A. Hauchecorne, N. Mzé, and P. Keckhut (2015), Seasonal variation of gravity wave activity at midlatitudes from 7 years of COSMIC GPS and Rayleigh lidar temperature observations, Geophys. Res. Lett., 42, doi:10.1002/2014GL062891.

Kursinski, E. R., et al. (1997), Observing Earth's atmosphere with radio occultation measurements using the Global Positioning System, J. Geophys. Res., 102, 23,429–23,465.

Lange, M., and C. Jacobi (2003), Analysis of gravity waves from radio occultation measurements, in First CHAMP Mission Results for Gravity, Magnetic and Atmospheric Studies, edited by C. Reigber, H. Lьhr, and P. Schwintzer, pp. 479–484, Springer, Berlin.

Lindzen, R. S., and J. R. Holton (1968), A theory of the Quasi-Biennial Oscillation, J. Atmos. Sci., 25, 1095–1107.

Marquardt, C., and S. B. Healy (2005), Measurement noise and stratospheric gravity wave characteristics obtained from GPS occultation data, J. Meteorol. Soc. Jpn., 83, 417–428.

Maury P, Claud C, Manzini E, Hauchecorne A, Keckhut P (2016), Characteristics of stratospheric warming events during Northern winter, (in press), doi :<10.1002/2015JD024226>

McDonald, A. J. (2012), Gravity wave occurrence statistics derived from paired COSMIC/FORMOSAT3 observations, J. Geophys. Res., 117, D15106, doi:10.1029/2011JD016715

McFarlane, N. A. (1987), The effect of orographically excited gravity wave drag on the general circulation of the lower stratosphere and troposphere, J. Atmos. Sci., 44, 1775–1800.

Ratnam, M. V., G. Tetzlaff, and C. Jacobi (2004), Global and seasonal variations of stratospheric gravity wave activity deduced from the CHAMP/GPS satellite, J. Atmos. Sci., 61, 1610– 1620.

Šácha, P., Kuchař, A., Jacobi, C., and Pišoft, P.: Enhanced internal gravity wave activity and breaking over the northeastern Pacific–eastern Asian region, Atmos. Chem. Phys., 15, 13097-13112, doi:10.5194/acp-15-13097-2015, 2015

Šácha, P., Foelsche, U., and Pišoft, P.: Analysis of internal gravity waves with GPS RO density profiles, Atmos. Meas. Tech., 7, 4123-4132, doi:10.5194/amt-7-4123-2014, 2014.

Scherllin-Pirscher, B., A.K. Steiner, G. Kirchengast, Y.-H. Kuo, and U. Foelsche (2011) Empirical analysis and modeling of errors of atmospheric profiles from GPS radio occultation, Atmos. Meas. Tech., 4, 1875-1890, doi:10.5194/amt-4-1875-2011.

Schmidt, T., et al. (2008), Global gravity wave activity in the tropopause region from CHAMP radio occultation data, Geophys. Res. Lett., 35, L16807, doi:10.1029/2008GL034986.

Schmidt, T., et al. (2010), Observational characteristics of the tropopause inversion layer derived from CHAMP/GRACE radio occultations and MOZAIC aircraft data, J. Geophys. Res., 115, D24304, doi:10.1029/2010JD014284.

Schmidt, T., P. Alexander, and A. de la Torre (2016), Stratospheric gravity wave momentum flux from radio occultations, J. Geophys. Res. Atmos., 121, 4443–4467, doi:10.1002/2015JD024135.

Steiner, A. K. and Kirchengast, G.: Gravity Wave Spectra from GPS/MET Occultation Observations, J. Atmos. Ocean. Tech., 17, 495–503, doi:10.1175/1520-0426(2000)017<0495:GWSFGM>2.0.CO;2, 2000.

Tsuda, T., M. Nishida, C. Rocken, and R.H. Ware (2000), A global morphology of gravity wave activity in the stratosphere revealed by the GPS occultation data (GPS/MET), J. Geophys. Res., 105, 7257–7273, doi:10.1029/1999JD901005.

Tsuda, T., M. V. Ratnam, P. T. May, M. J. Alexander, R. A. Vincent, and A. MacKinnon (2004), Characteristics of gravity waves with short vertical wavelengths observed with radiosonde and GPS occultation during DAWEX (Darwin Area Wave Experiment), J. Geophys. Res., 109, D20S03, doi:10.1029/2004JD004946.

Wang, L., and M. A. Geller (2003), Morphology of gravity-wave energy as observed from 4 years (1998–2001) of high vertical resolution U.S. radiosonde data, J. Geophys. Res., 108(D16), 4489, doi:10.1029/2002JD002786

Wang, L., and M. J. Alexander (2009), Gravity wave activity during stratospheric sudden warmings in the 2007–2008 Northern Hemisphere winter, J. Geophys. Res., 114, D18108, doi:10.1029/2009JD011867.

Wang, L., and M. J. Alexander (2010), Global estimates of gravity wave parameters from GPS radio occultation temperature data, J. Geophys. Res., 115, D21122, doi:10.1029/2010JD013860.

Wickert J., Schmidt T., Michalak G., Heise S., Arras C., Beyerle G., Falck C., König R., Pingel D., and Rothacher M.:GPS radio occultation with CHAMP, GRACE-A, SAC-C, TerraSAR-X, and FORMOSAT-3/COSMIC: brief review of results from GFZ, in: New horizons in occultation research, edited by: Steiner, A., Pirscher, B., Foelsche, U., Kirchengast, G., Springer, Berlin Heidelberg, 3–15, doi:10.1007/978-3-642-00321-9, 2009.

Wright, C. J., M.B. Rivas, and J. C. Gille (2011), Intercomparisons of HIRDLS, COSMIC and SABER for the detection of stratospheric gravity waves, Atmos. Meas. Tech., 4, 1581-1591, doi:10.5194/amt-4-1581-2011.

Wu, D. L., et al. (2006), Remote sounding of atmospheric gravity waves with satellite limb and nadir techniques, Adv. Space Res., 37, 2269–2277, doi:10.1016/j.asr.2005.07.031.

7. List of Acronyms

CDR	Climate Data Record
CHAMP	CHAllenging Mini-Satellite Payload
COSMIC	Constellation Observing System for Meteorology, Ionosphere, and Climate
ECMWF	European Centre for Medium-range Weather Forecasts
EOS	Earth Observing Satellite
EUMETSAT	EUropean organisation for the exploitation of METeorological SATellites
GNSS	Global Navigation Satellite System
GPS	Global Positioning System (USA)
GRACE	Gravity Recovery and Climate Experiment
GRAS	GNSS Receiver for Atmospheric Sounding (on Metop)
GW	(atmospheric) Gravity Wave
HD	Horizontal Detrending
HDF	Hierarchical Data Format
HIRDLS	High Resolution Dynamics Limb Sounder
LEO	Low Earth Orbiting (satellite)
Metop	Meteorological Operational Satellite
NetCDF	Network Common Data Form
NWP	Numerical Weather Prediction
PCD	Product Confidence Data
RO	Radio Occultation
ROM SAF	Radio Occultation Meteorology (ROM) Satellite Application Facility (SAF) (EUMETSAT)
ROPP	Radio Occultation Processing Package
QBO	Quasi-Biennial Oscillation
SABER	Sounding of the Atmosphere using Broadband Emission Radiometry
SACC	Satélite de Aplicaciones Científicas-C
SSW	Stratospheric Sudden Warming
TIMED	Thermosphere Ionosphere Mesosphere Energetics and Dynamics
VD	Vertical Detrending